Development of Ni-Fe based ternary metal hydroxides as highly efficient oxygen evolution catalysts in AEM water electrolysis for hydrogen production

Adeline Loh[a], Xiaohong Li[a*], Oluwadamilola O. Taiwo[b], Farid Tariq[b], Nigel P. Brandon[b], Peican Wang, Ke Xu[c], Baoguo Wang[c]

[a] *Renewable Energy Group, College of Engineering, Mathematics and Physical Sciences, University of Exeter, Penryn Campus, Cornwall TR10 9FE, UK*

[b] *Earth Science and Engineering, Imperial College London, SW11 2AZ, UK*

[c] *Department of Chemical Engineering, Tsinghua University, Beijing 100084, China*

Abstract

A number of mixed metal hydroxide oxygen evolution reaction (OER) catalysts i.e. Ni-Fe, Ni-Co, Ni-Cr, Ni-Mo, Ni-Fe-Co, Ni-Fe-Mo and Ni-Fe-Cr were prepared by cathodic electrodeposition and characterised by SEM, TEM, EDS, XPS and micro X-CT. The compositions of selected catalysts were optimised to give lower OER overpotentials in alkaline media. Further optimisation of Ni-Fe based ternary metal hydroxide catalysts such as Ni-Fe-Co and Ni-Fe-Mo was carried out, showing improved performance at high current densities up to 1 A cm^{-2} in 1 M NaOH, 333 K. The influence of electrodeposition parameters such as current density, pH, electrodeposition time and temperature on the electrocatalytic performance of ternary Ni-Fe-Co metal hydroxide was further investigated and optimised. The durability of the optimised catalyst was tested at a current density of 0.5 A cm^{-2} in an anion exchange membrane (AEM) water electrolyser cell at 4 M NaOH, 333 K, demonstrating stable performance over 3.5 h.

Keywords: oxygen evolution reaction; NiFeCo ternary metal hydroxide; cathodic electrodeposition; anion exchange membrane (AEM); water electrolyzer; hydrogen production

*Corresponding author. *Email:* X.Li@exeter.ac.uk Tel: 0044 (0)1326 255769

1. Introduction

Water electrolysis coupled with renewable energy sources is considered a zero-carbon pathway to the production of hydrogen, without the consumption of fossil fuels or CO_2 emissions. Traditional alkaline electrolysis is a mature technology, producing hydrogen at low capital cost due to the use of non-precious metal catalysts but suffers with problems such as low current density, low gas purity and low system efficiency [1]. These shortcomings have led to the development of acidic proton exchange membrane (PEM) water electrolysers. However, although PEM cells demonstrate fast response, high gas purity and system efficiency [2], they offer expensive hydrogen due to heavy dependence on precious metal catalysts and costly proton exchange membranes and which limit the large-scale commercialisation of these systems [3]. Having emerged in the last decade, anion exchange membrane (AEM) electrolysers possess the merits of the zero-gap configuration of PEM electrolysers whilst allowing the use of non-precious metal catalysts and less costly cell components resulting in the promise of cheaper hydrogen production [4].

Previous research work has indicated that the anodic oxygen evolution reaction is a key reaction in water electrolysis because the anode overpotential is always significantly larger than the cathode overpotential [5, 6]. The mechanism of oxygen evolution comprises of several intermediate single electron states, due to its kinetically unfavourable transfer of four electrons for the production of one molecule of oxygen. This leads to a build-up of energy barriers and thus slow reaction kinetics, which is seen as the major source of energy loss. As such, the development of inexpensive and efficient OER catalysts is crucial to achieving higher cell efficiencies.

Numerous materials have been studied for their OER activity and great interest in metal-based electrocatalysts have been shown [7]. In the alkaline environment, first-row transition metal compounds demonstrate high catalyst activity for OER whilst remaining low in cost and

corrosion resistant in highly alkaline environments [8, 9]. For instance, Ni, Fe and Co based electrocatalysts have each displayed the ability of reducing OER overpotential [10-12]. Such transition metal oxides, hydroxides and oxyhydroxides have been thoroughly investigated and activities for these catalysts have been benchmarked [13, 14] with the general trend in reactivity found to be Ni > Co > Fe [14-17]. These comparative studies propose nickel to be the most efficient catalyst for OER based on adsorption energies or bond strengths of the reaction intermediates [16, 18]. As a result, studies have been carried out to further enhance the activity of these hydroxides or oxyhydroxides through the incorporation of other transition metals, which have been shown to have a significant effect on the electronic properties of $Ni(OH)_2$ [19, 20]. The fabrication and optimisation of mixed metal oxide and hydroxide catalysts are based on Brewer's theory that a stronger d-d-intermetallic bonding between the intermetallic phases results in a weaker intermediate adsorptive bond (e.g. M-OH, M-H) in the rate determining step [21]. This allows for more rapid dissociation, faster reaction rate and better intrinsic catalyst activity overall. Synergism in mixed hypo-hyper-d electronic oxide catalysts depend on the composition ratio and the effect of the interaction between the mixed metals produces an optimal composition for maximum activity [22].

The introduction of 'impurities' into a Ni metal oxide can thereby encourage increases in conductivity, alter the intermediate bonding energy for better catalysis and potentially provide more favourable active sites for intermediates to bind to [23-25]. Further, the combination of multiple first-row transition metals provides the advantage of multiple oxidation states in the operating potential range. As investigated by Stahl et al. [26, 27], catalysts containing Ni, Fe and a third metal show higher OER activity with good reproducibility compared to binary Ni-based oxides and studies on ternary Ni-Fe based electrocatalysts report stable OER performance required for alkaline electrolysis [28-30].

Based on these sources, Ni-Fe based ternary metal catalysts are proposed to be potential catalyst candidates with enhanced OER activity.

There are several methods through which transition metal oxides and hydroxides can be prepared such as chemical [31] or electrochemical precipitation [32], hydrothermal [33, 34], and solvothermal.[35] The method of electrodeposition is particularly versatile as it can produce diverse metal oxide and hydroxide deposit morphologies and properties, which are a function of the electrodeposition conditions such as electrodeposition potential or current, electrolyte pH, composition and additives.

Herein, we report a comprehensive study on electrodeposited Ni-based binary metal hydroxide catalysts Ni-Fe, Ni-Co, Ni-Cr and Ni-Mo, as well as Ni-Fe based ternary metal hydroxide catalysts Ni-Fe-Co, Ni-Fe-Mo and Ni-Fe-Cr for OER activity. Electrochemical measurements were carried out with a microelectrode in order to minimise ohmic drop and ensure a more reliable comparison of the catalysts at high current densities of interest for water electrolysers (e.g. > 1 A cm^{-2}). Characterisation techniques such as SEM, TEM, XPS and X-ray CT were employed to study the electrodeposited catalysts and the effect of electrodeposition parameters on the properties of these metal hydroxide deposits. The catalytic performance of ternary Ni-Fe based hydroxide, Ni-Fe-Co, for oxygen evolution reaction, in particular, is further investigated and discussed.

2. Experimental procedures

2.1. Synthesis of binary and ternary metal hydroxide catalysts

Metal salts: nickel (II) sulphate hexahydrate, $NiSO_4.6H_2O$ (Sigma-Aldrich, ≥98%), iron (II) sulphate heptahydrate, $FeSO_4.7H_2O$ (Sigma Aldrich, ≥99.0%), chromium (III) sulphate hydrate, $Cr(SO_4)_3.xH_2O$ (Sigma Aldrich) , cobalt (II) sulphate heptahydrate, $CoSO_4.7H_2O$ (Alfa Aesar, 98%), ammonium molybdate tetrahydrate, $(NH_4)_6Mo_7O_{24}.4H_2O$ (Alfa Aesar,

99%) and ammonium sulphate, $(NH_4)_2SO_4$ (Sigma Aldrich, ≥99.%), were used as received. Electrodeposition of the catalyst samples was carried out in a small undivided glass cell (approx. 20 cm^3) equipped with a water jacket and polymer lid connected to a Grant TC120 series heated circulating water bath. A stainless steel (SS) microelectrode, Pt mesh and Hg/ HgO in 1 M NaOH were used as working, counter and reference electrodes respectively. The microelectrode was made of an SS wire (Goodfellow, purity 99.0 %, 25 μm diameter) sealed in glass, giving a cross-sectional area roughly 5 x 10^{-6} cm^2. The microelectrode tip was polished with alumina slurry (MicroPolish, Buehlar) of 1.0 μm and 0.05 μm consecutively on Microcloth (Buehlar) and sonicated in DI H_2O for 15 mins prior to each run.

Electrodeposition solutions to prepare the metal hydroxide catalysts consisted of aqueous solutions of 18 mM binary (i.e. Ni-Fe, Ni-Co, Ni-Cr, Ni-Mo) and ternary (i.e. Ni-Fe-Co, Ni-Fe-Cr and Ni-Fe-Mo) transition metal sulphate salt + 25 mM ammonium sulphate. The cathodic deposition of the various single and mixed metal hydroxides was conducted under galvanostatic control using current densities between 0.1 - 0.5 A cm^{-2} and deposition times of 60 to 300 s at pH values of 2 to 6 and temperatures of 295-343 K. Standard parameters for electrodeposition was a cathodic current of 0.2 A cm^{-2} for 120 s at ambient temperature unless otherwise stated.

2.2. Structural and morphological characterization

The surface morphology and composition of the various samples was characterised with an SEM-EDS (FEI Quanta 650 FEG) operated at 5 kV accelerating voltage. The percentage composition of transition metals at the catalyst surface was determined with EDX, from samples deposited on carbon polymer plate (BMA5, Eisenhuth) with a working area of ≈0.126 cm^2 masked out with polypropylene (Avon) tape. Carbon polymer plate was used as an electrode substrate to allow the composition of the deposit to be determined without influence

from the substrate. Samples were prepared on carbon polymer plate in the same manner for X-ray photoelectron spectroscopy (XPS, Thermo Fisher, ESCALAB 250Xi) measurements carried out with a monochromatic Al Kα source over energy range of 0 to 1350 eV with pass energy of 30.0 eV, step size of 0.05 eV and X-ray spot size of 500 μm. All spectra were analysed with XPSPEAK 4.1 software using NIST XPS database [36]. TEM analysis was conducted with a JEM-2100 LaB6 200 kV and samples were directly deposited onto 3.05 mm diameter Cu grid of 100 square mesh (AGG2100C, Agar Scientific) for characterisation.

The microstructure of the catalyst films was studied with 3D tomography carried out with a lab-based GE Phoenix Nanotom S X-ray tomography machine (GE, Boston, USA). The samples were deposited onto a polished glassy carbon disc, 2 mm diameter (Alfa Aesar) for a suitable field of view. Samples were aligned perpendicular to the beam prior to imaging. Each deposition was scanned to acquire a total of 2401 projections at 100 kV and 260 μA and the acquired images were reconstructed with final resolution between 0.9 and 1.5 μm. Subsequent analysis was carried out with ImageJ and visualised using Avizo 9 (Fisher-Scientific, Bordeaux, France).

2.3. Electrochemical measurements

Electrochemical measurements were performed with a Bio-logic potentiostat and EC-lab software. Cyclic voltammograms were obtained in potential range of 0.1 to 0.7 V at a scan rate of 100 mV s^{-1} and slow scan linear sweep voltammograms were obtained for anodic potentials of 0.45 to 0.8 V at a scan rate of 1 mV s^{-1}. All current densities in this work are reported as a function of the electrode geometric area. The samples were tested in a standard three-electrode glass cell with an inbuilt water jacket and polymer lid. The temperature of the electrolyte was calibrated before each run with a water bath to 333 K. In both set-ups of catalyst deposition and OER performance testing, Pt mesh and Hg/ HgO in 1 M NaOH were used as a

counter electrode and reference electrode, respectively. The working electrode was orientated upwards into the cell to facilitate the release of O_2 bubbles and prevent the build-up of bubbles on the microelectrode surface. All experiments were carried out in static electrolyte and reported results were obtained after several scans when a stable response was reached.

Commercial OER electrodes were used as received and tested under the same conditions as the metal hydroxide catalyst-coated electrodes for comparison. The commercial OER electrode (Type 1.7, Magneto special anodes, B.V.) was an expanded Ti mesh 1.3 to 1.6 mm thick, coated with Ru-Ir mixed metal oxides.

2.4. Stability tests in an AEM water electrolyer cell

The optimised catalyst samples were tested in a zero-gap alkaline water electrolyser to demonstrate stability. This electrolyser cell was assembled with two mesh electrodes (working area ≈ 9 cm^2) on either side of an anion exchange membrane (A201, Tokuyama Corp. Japan). The cathode was expanded Ni mesh (DeXmet Corp, 4Ni 6-040) and the anode was expanded SS mesh (DeXmet Corp, 4SS 5-050) coated with cathodically deposited catalyst samples.

Binary Ni-Fe hydroxide and ternary Ni-Fe-Co hydroxide catalysts were prepared by cathodic electrodeposition onto SS expanded mesh using the optimised deposition parameters. To account for the variation in current density distribution across a solid planar versus mesh working electrode, two pieces of Pt mesh counter electrodes were placed on either side of the SS mesh to facilitate a well-distributed electric field for electrodeposition and the deposition time was extended to ensure that the mesh was sufficiently coated with catalyst. In addition, since H_2 gas can be evolved as a side reaction during electrodeposition, the rate of mass transfer becomes more significant over a larger electrode area [37]. Hence, to ensure a more uniformly coated SS mesh; the deposition solution was also stirred at 100 rpm to prevent H_2 bubbles from obstructing the surface to be coated.

During testing, 4 M NaOH electrolyte was continuously pumped through the cell at a flow rate of 250 mL min^{-1} by a peristaltic pump (Watson Marlow, UK) to prevent a build-up of H_2 or O_2 bubbles at the electrodes. The electrolyser was operated at a current density of 0.5 A cm^{-2} for 3.5 h for the stability tests. The selection of electrolyte concentration for AEM testing was influenced by conductivity, viscosity and O_2 diffusivity. As indicated in **Fig. S1**, 4 M NaOH supports high electrolyte conductivity for better cell performance and has a reasonable viscosity and O_2 diffusivity for rapid removal of the O_2 bubbles produced. The Tokuyama A201 membrane is also stable at the chosen electrolyte concentration.

3. Results and discussion

3.1. Unary metal hydroxide catalysts

Fig. 1 presents the cyclic voltammogram of $Ni(OH)_2$ on SS microelectrode in 1 M NaOH at 333 K at a potential scan rate of 100 mV s^{-1} between 0.1 and 0.7 V. The $Ni(OH)_2$ layer was cathodically deposited onto the polished SS microelectrode from 18 mM nickel sulphate solution at 0.2 A cm^{-2} for a period of 120 s. When polarised to positive potentials, the $Ni(OH)_2$ oxidises and oxygen evolution occurs on the oxidised nickel surface. The voltammogram has a well-formed anodic peak at 0.49 V and corresponding cathodic peak at 0.42 V which relates to the surface conversion between $Ni(OH)_2$ and NiOOH [38]. This is described by reaction (1).

$$Ni(OH)_2 + OH^- \leftrightharpoons NiOOH + H_2O + e^- \quad (1)$$

The rapidly increasing anodic peak at potentials more positive than 0.6 V represents the evolution of oxygen. This is described by reaction (2).

$$4OH^- \rightarrow 2H_2O + O_2 + 4e^- \quad (2)$$

These two anodic reactions theoretically occur around the same potentials, however due to the sluggish kinetics of the oxygen evolution reaction, the experimental onset potential of reaction (2) usually takes place at more positive potentials. From **Fig. 1**, it is observed that the

presence of $Ni(OH)_2$ on the surface of the microelectrode enables OER to occur at high current densities up to 2 A cm^{-2}.

The cyclic voltammograms of five unary hydroxide catalysts are displayed in **Fig. 2a**. It is seen that the OER performance of these unary hydroxide catalysts can be ranked in order of Co > Ni > Cr > Fe > Mo. Fig**. 2b** illustrates slow scan linear voltammograms of these unary hydroxide catalysts at 1 mV s^{-1}, giving details of OER performance, where Ni and Co unary hydroxides clearly demonstrate the best overall performance with lowest overpotentials. The OER overpotential values for the unary hydroxides are recorded in **Table 1**. At low current densities, unary Cr hydroxide reports better catalytic performance than Fe and Mo unary hydroxides. However, at current densities greater than 1 A cm^{-2}, the catalytic performance of Fe unary hydroxide surpasses that of Cr unary hydroxide. It is worth noting that the $Ni(OH)_2$ oxidation peaks observed in **Fig. 2a** are absent in **Fig. 2b** because current is proportional to scan rate. At low scan rates of 1 mV s^{-1} in **Fig. 2a** *vs* 100 mV s^{-1} in **Fig. 2a**, the flux of reactants to the electrode surface through the diffusion layer is much slower therefore less current is detected.

Due to the difficulty in identifying the reaction intermediates present on the metal oxide surface, the Tafel slope value is recognised as a kinetic parameter which, to a certain extent, can be used to suggest the rate determining step of the proposed pathway. Assuming a single-site mechanism under alkaline conditions where S is a single site on the surface, a proposed reaction mechanism is written as [39, 40]

	Associated Tafel slope value, $\partial V / \partial \ln I$ [41]	
$S + OH^- \leftrightarrow S\text{-}OH + e^-$	2RT/F	(3)
$S\text{-}OH + OH^- \leftrightarrow S\text{-}O + H_2O + e^-$	2RT/3F	(4)
$2S\text{-}O \leftrightarrow 2S + O_2$	RT/4F	(5)
$S\text{-}O + OH^- \leftrightarrow S\text{-}OOH + e^-$	2RT/5F	(6)
[a]$S\text{-}OOH + OH\text{-} \leftrightarrow S + H_2O + O_2$	RT/4F	(7)

[a]$S\text{-}OOH + OH^- \leftrightarrow S\text{-}OO^- + H_2O$
$S\text{-}OO^- \leftrightarrow S + O_2 + e^-$

The Tafel slope, b value is given by equation (8),

$$\text{Tafel slope, b} = \frac{2.303\,RT}{(1-\alpha)F} \qquad (8)$$

where α is the transfer coefficient, R is 8.3145 J mol^{-1} K^{-1}, F is 96485 C mol^{-1} and T is absolute temperature (298 K). From **Fig. 2c** the Tafel slope values of unary hydroxides of Ni, Co, Fe and Cr (reported in **Table 1**) are found to be between 38 and 43 mV dec^{-1} indicating that these hydroxides have a similar OER mechanism. Generally, a Tafel slope value of ~40 mV dec^{-1} (2RT/3F) corresponds to an OER mechanism where the second electron step (equation 4) is rate determining [10, 16]. Whilst a Tafel slope value of 50 mV dec^{-1} (4RT/5), as reported for Mo unary hydroxide, which is not found in this mechanism indicates that the rate determining step is likely to be a chemical step [42].

The morphology, microstructure, and surface oxidation state of the unary metal hydroxide catalyst films were characterised with SEM, TEM, micro X-CT, and XPS. SEM images in **Fig. 3a (i)**, **3b (i)** and **3c (i)** reveal that the deposit films possess rough and porous morphology. Based on equation (9), thick insoluble hydroxide layers are deposited on the surface by cathodic generation in a nickel-based electrolyte [43].

$$Ni^{2+} + 2H_2O + 2e^- \rightarrow Ni(OH)_2 + H_2 \qquad (9)$$

At high deposition current densities, the potential response is much more negative than the standard reduction potential of water, which occurs as a side reaction of the cathodic electrodeposition, resulting in a small loss of current efficiency to the evolution of hydrogen. The production of hydrogen during electrodeposition leads to the uneven morphology of the obtained deposits.

Under high resolution TEM, the deposit from Ni sulphate solution is composed of interconnected platelets forming dendritic structures (**Fig. 3a (ii)**) while the deposit from Fe sulphate solution consists of densely packed crumpled layers of nanosheets (**Fig. 3b (ii)**), and the deposit from Co sulphate solution displays aggregated nanoflower-like structures (**Fig. 3c**

(ii)). The electron diffraction patterns of these samples are composed of diffused rings, which indicate that the deposits are amorphous or of low crystallinity. This agrees well with initial XRD results, which exhibited broad and unresolved peaks. The ring diameters of diffraction pattern in **Fig. 3a (iii)** are indexed to the lattice planes of hexagonal $Ni(OH)_2$ (JCPDS 00-002-1112, space group: P-3m1 (164) with lattice constants a = 3.11 and c = 4.66). The rings in **Fig. 3b (iii)** and **Fig. 3c** (**iii)** are found to correspond to standard d_{hkl} patterns for orthorhombic FeOOH (COD 9003076, space group: Pbnm (62) with lattice constants a = 4.63, b = 9.99, c = 3.04, a/b =0.463 and c/b =0.304) and hexagonal $Co(OH)_2$ (JCPDS 00-030-0443, space group: P-3m1 (164) with lattice constants a = 3.18 and c = 4.65) respectively [44, 45]. The detection of FeOOH is proposed to be due to the spontaneous oxidation of the electrodeposited $Fe(OH)_2$ to FeOOH in the presence of oxygen [46, 47].

The microstructures of the catalyst films of unary Ni, Fe and Co hydroxides are observed to be distinct from one another as seen in **Fig. S2a**, **b and c** respectively. The unary Ni hydroxide deposit (**Fig. S2a**) has an uneven granular structure and from the corresponding histogram, the thickness of the Ni-based catalyst film ranges from 1.7 to 49 μm, with the largest proportion of the film at a thickness of 11.6 - 12 μm and approximately half of the film is 8.2 - 21.3 μm thick. The unary Fe hydroxide deposit in **Fig. S2b**, is a thin film of relatively consistent thickness throughout, with several cracks in its microstructure. From the corresponding histogram, the range of thicknesses is only between 2.3 μm and 16.2 μm and a large percentage of the catalyst film is 7.4 μm thick. The unary Co hydroxide deposit is composed of separated disc-like structures which are not well adhered to the substrate in some areas. The corresponding histogram for the deposit shows that the thickness ranges between 2.5 and 30.5 μm, although a large proportion of the film is less than 10.5 μm thick. The histogram also reveals that the majority of the unary Co hydroxide deposit is 8.4 μm thick.

The surface areas and volumes of the three dimensional structures were quantified and

surface area to volume ratios of each catalyst film are displayed in **Table S1**. Comparing these values against the catalytic performance of the unary, binary and ternary hydroxides reveals that the catalyst film composition is more important than surface area for obtaining higher OER activity. Although the surface area per volume ratio value of unary Fe hydroxide is almost twice that of unary Ni hydroxide, the OER overpotential of the unary Fe hydroxide catalyst is 50 mV greater than unary Ni hydroxide at 0.1 A cm^{-2}, and 52 mV greater at 0.5 A cm^{-2}. Equally, the surface area per volume ratio of unary Co hydroxide is almost twice that of unary Ni hydroxide, but its overpotential for OER is only 6 mV less than unary Ni hydroxide at 0.1 A cm^{-2} and 13 mV less at 0.5 A cm^{-2}.

XPS measurements give further insight into the components present in these samples as well as the oxidation state of each transition metal element. The spectra for Ni2p is shown in **Fig. 4a**, with peaks for p orbitals $2p_{3/2}$ and $2p_{1/2}$ centred at 856.7 eV and 874.5eV respectively. The spin orbit separation of these two peaks is 17.8 eV, which is characteristic of $Ni(OH)_2$ [48]. The O1s spectrum of this sample (**Fig. 4d**) was fitted with peaks for lattice H_2O, M-O and M-OH bonds. The peak at binding energy 532 eV is characteristic of the OH^- bound hydroxide group for $Ni(OH)_2$, and the peak at approx. 530 eV is characteristic of O^{2-} of M-O bond for NiO. Overall, the shapes and positions of the Ni2p and O1s peaks match those of standard XPS spectra for Ni^{2+} [49-52]. The signal areas of M-O and M-OH peaks in the O1s spectra also correspond well with that of NiO and $Ni(OH)_2$ in the Ni2p spectrum confirming that the sample is largely composed of $Ni(OH)_2$.

The Fe2p spectrum (**Fig. 4b**) shows peaks for $Fe2p_{3/2}$ and $Fe2p_{1/2}$ at 711.5 eV and 724.9 eV, which gives a spin separation of 13.4 eV, characteristic of both FeOOH and Fe_2O_3 [53]. The broad satellite peak at approx. 720 eV in this spectra is characteristic of Fe of oxidation state 3 [54], and $BE_{O1s} - BE_{Fe2p3/2}$ = 181.1 eV gives further evidence of the presence of Fe^{3+} [55]. The accompanying O1s spectra (**Fig. 4d**) has a peak at 531.6 eV from M-OH of FeOOH

and a shoulder peak at 530.2 eV for M-O of Fe_2O_3, consistent for metal oxyhydroxide of Fe^{3+}. Overall, the Fe2p and O1s spectra matches that of FeOOH in the literature [56-58].

The Co2p spectrum in **Fig. 4c** displays peaks for $Co2p_{3/2}$ and $Co2p_{1/2}$ at binding energies of 781.0 eV and 797.0 eV, resulting in a spin separation of 16.0 eV, which is characteristic of $Co(OH)_2$ [59]. Furthermore, the prominent satellite peaks which accompany the Co2p peaks indicate that high-spin Co^{2+} species is dominant in the deposit as these satellite peaks are usually weak or absent for low-spin Co^{3+} species [60, 61]. The accompanying O1s spectrum (**Fig. 4d**) has a peak at 531.2 eV which is characteristic of the M-OH bond in $Co(OH)_2$ [62, 63]. The signal areas of M-O and M-OH in O1s spectrum correspond well to that of the Co2p spectrum confirming that Co^{2+} species is present and the sample is largely composed of $Co(OH)_2$.

3.2. Binary metal hydroxide catalysts

Binary hydroxides Ni-Fe, Ni-Co, Ni-Mo and Ni-Cr were investigated in the same manner and their OER overpotentials and Tafel slope values are summarised in **Table 1.** The electrodeposition bath compositions of selected samples and the corresponding atomic percentages of the metal elements present as determined by EDX are displayed in **Table S2.**

Cyclic voltammograms of catalyst hydroxide films synthesised from deposition solutions with varying molar percentages of Ni and Fe are given in **Fig. 5a**. EDX analysis of an electrodeposited Ni-Fe catalyst in **Fig. S3** gives evidence that the elements are well distributed throughout the layer. There is a clear trend whereby the anodic peak potentials for reaction (1) of the mixed catalyst films shift to more positive potentials in response to increases in molar percentage of Fe in the deposition solution. This demonstrates that the Fe^{3+} in the deposit oxidises at more positive potentials than Ni^{2+}. The sample from deposition solution containing 25% Fe gives the lowest OER overpotential of 292 mV at 0.1 Acm^{-2} (**Fig. 5b**), which has also

been reported by several other studies [17, 64, 65]. Aside from the shift in the $Ni^{2+/3+}$ anodic peak, the presence of 25% and 50% Fe in the deposition solution also appears to enable OER (reaction (2)) to occur at less positive potentials, thereby reducing the overpotential. Tafel slopes, *b*, of these samples are plotted in **Fig. 5c**. The Tafel slope values of Ni and Fe unary metal hydroxides are 40 mV dec^{-1} and 42 mV dec^{-1} respectively which agree with reported values [16], whilst the Tafel slope value of catalyst from the deposit solution containing 25% Fe is 48 mV dec^{-1}. This slight increase in Tafel slope value indicates that the addition of Fe has brought about a change in the OER mechanism [16], either in the rate determining step of the same reaction pathway or in the adsorption conditions of the reaction intermediates [42].

Of the binary Ni-Co hydroxides tested, the lowest OER overpotential recorded is 295 mV at 0.1 A cm^{-2} for the catalyst from a 75% Co deposit solution. The OER overpotential of Ni-Co hydroxides is seen to increase gradually with increasing Ni content in the deposit solution. Binary Ni-Mo hydroxides are also observed to be more active OER catalysts compared to unary Mo hydroxide. The electrodeposition solutions of 50% and 75% Mo produce catalysts that have lower OER overpotentials compared to unary Ni hydroxide, and the catalyst produced from deposition solution of 50% Mo reported the lowest OER overpotential of the Ni-Mo binary hydroxides tested. EDX measurements of the sample's surface (**Table S2**), however, shows that it is actually composed of 75% Ni and 25% Mo, indicating that Ni is deposited preferentially to Mo. Of the binary Ni-Cr hydroxides tested, the lowest OER overpotential was reported for the catalyst synthesised from a deposition solution of 25% Cr. Catalysts synthesised from deposition solutions of 50 – 100% Cr however, reported much higher OER overpotentials. This is supported by Diaz-Morales et al.'s computational study [19] of doped Ni oxyhydroxides, which proposed that Ni is the active site on Cr-doped Ni oxyhydroxide. Therefore, a Ni-Cr hydroxide from a deposit solution with a larger percentage of Ni is likely to have more OER sites.

From the experimental results, the Ni-based binary metal hydroxides ranked according to their OER overpotential values at 0.1 A cm^{-2} are Ni-Fe < Ni-Cr < Ni-Co < Ni-Mo; and at 0.5 A cm^{-2} this is Ni-Fe ≈ Ni-Co < Ni-Cr < Ni-Mo, these are similar to the trends observed in benchmarking studies of Ni-based metal oxides [66], hydroxides [17], and oxyhydroxides [19]. **Table S2** reports the loading of the samples as determined by Faraday's law of electrolysis and loading per unit area for all metal hydroxide catalysts is approx. 0.007 g cm^{-2}. The OER performances of the binary hydroxides according to their overpotentials at ≥ 50 A g^{-1} are ranked Ni-Co < Ni-Fe < Ni-Cr < Ni-Mo (**Fig. S4**), which also follows the same trend reported at 0.5 A cm^{-2}.

TEM and X-ray micro CT were used to study the effect of depositing more than one transition metal hydroxide on the morphology of binary and ternary hydroxides of Ni-Fe, Ni-Co and Ni-Fe-Co. The TEM micrograph of Ni-Fe binary hydroxide in **Fig. 6a** displays the dendritic structure of unary Ni hydroxide covered by nanosheets of unary Fe hydroxide. From **Fig. S2d**, this binary hydroxide is composed of large angular deposit fragments of fairly consistent thickness. The accompanying histogram indicates that although the film has a range of thicknesses between 2.4 and 30 μm, the bulk of the film is 8.4 μm which is slightly greater than the average thickness of unary Fe hydroxide, but much less than that of unary Ni hydroxide. The range of thicknesses displayed in the histogram of the binary Ni-Fe hydroxide is also smaller than that for Ni unary hydroxide. These observations suggest that in Ni-Fe binary hydroxide, the unary Fe hydroxide coats the dendritic structure of unary Ni hydroxide, thereby obstructing the growth of the catalyst layer and helping the deposit to maintain an even thickness.

In **Fig. 6b**, the morphology of Ni-Co binary hydroxide reveals a dendritic structure of unary Ni hydroxide encased by the nanoflower-like structures of unary Co hydroxide. In **Fig. S2e**, the curved disc-like structures, which are characteristic of unary Co hydroxide, are

observed in the microstructure of the catalyst film. The substrate surface is however more sparsely covered by the binary hydroxide deposit compared to its unary hydroxide counterparts. The corresponding histogram for the Ni-Co binary hydroxide catalyst deposit indicates that the majority of the film is 17.7 μm thick, which is much thicker than that of either unary Ni, or Co hydroxide catalyst deposits. It is therefore likely that the Ni hydroxide provides a platform for the smaller discs of Co hydroxide to attach to, resulting in thicker deposits of binary Ni-Co hydroxide which do not adhere well to the substrate surface. It is noted that Co hydroxide does not have the same ability as Fe hydroxide to maintain homogeneity of the deposit structure.

XPS measurements of the binary metal hydroxide samples were carried out and results are displayed in **Fig. S5**. No significant peak shifts in the Ni, Fe and Co 2p spectra were detected which confirm the presence of $Ni(OH)_2$, $Co(OH)_2$ and FeOOH in the samples. There were, however, noticeable changes in the intensity of the peaks due to changes in quantities of the atoms present at these oxidation states.

3.3. Ternary metal hydroxide catalysts

The optimisation of the composition of ternary metal hydroxides is complicated by the preferential order of deposition [67] as observed in the EDX results. In order to account for the interactions between the binary metal hydroxides, the experimentally obtained optimal compositions of binary metal hydroxides of Ni-Fe, Ni-Co, Ni-Cr and Ni-Mo were initially used to determine the electrodeposition solution compositions of Ni-Fe based ternary metal hydroxides of Ni-Fe-Co, Ni-Fe-Mo and Ni-Fe-Cr, although other deposition compositions were also tested. All samples were cathodically deposited under the same conditions of 0.2 A cm^{-2} for 120 s onto the SS microelectrode tip and tested for OER performance under the same conditions.

Voltammograms of the optimal ternary metal hydroxides of Ni-Fe-Co, Ni-Fe-Mo and

Ni-Fe-Cr in comparison to unary Ni and binary Ni-Fe hydroxides are provided in **Fig. 6**. The overpotentials at current densities 0.1 and 0.5 A cm^{-2} and Tafel slope values for these hydroxide catalysts are tabulated in **Table 2**. The lowest overpotential at 0.1 A cm^{-2} is 265 mV, which is reported for Ni-Fe-Co ternary metal hydroxide. This is followed in ascending order by metal hydroxides of Ni-Fe-Mo > Ni-Fe-Cr > Ni-Fe > Ni. In **Fig. S4**, Ni-Fe-Co ternary hydroxide also displays consistently better OER performance compared to Ni-Fe-Mo ternary hydroxide at current densities up to 150 A g^{-1}. This implies that the combination of ternary metals, compared to binary or unary metals, has a greater effect on OER catalytic activity.

Several studies have been carried out to understand the effect of including Fe or Fe-Co to Ni on the intermetallic bonding in binary and ternary metal hydroxides, which report the promotion of electrocatalytic OER performance. For example, Louie and Bell [68] initially proposed that the addition of Fe to electrodeposited Ni films decreases the order of the crystal structure and reduces the average oxidation state of Ni. The same group observed with in operando high energy resolution fluorescence detection (HFRFD) mode X-ray absorption spectroscopy (XAS) measurements that the addition of up to 25% Fe in Ni-Fe based oxyhydroxides resulted in the substitution of Ni^{3+} for Fe^{3+} in the γ-NiOOH lattice, which enhanced the activities of the Fe^{3+} and Ni^{3+} sites [64]. Similarly, DFT calculations on phases of Co oxides showed that Co^{3+} in β-CoOOH was substituted by Ni^{3+} which was proposed to assist in lowering the overpotential considerably for OER [69]. A separate XAS study on Ni-Fe and Ni-Fe-Co oxide films proposed that the charge-transfer effects of Co present in the catalyst caused NiOOH to form at lower overpotentials thereby activating Fe sites, and the presence of Co also has an effect on the bond strength of the Fe-OH/ OOH reaction intermediate thereby optimising it for OER [70]. It is expected that more work using in operando characterisation will be especially helpful to understanding the effects of these metal dopants in binary and ternary hydroxide catalysts.

The TEM micrograph of ternary Ni-Fe-Co hydroxide in **Fig. 6c** presents the morphology of this catalyst as an interconnected network of Co unary hydroxide nanoflowers with platelets of Ni unary hydroxide dispersed throughout. The unary Fe hydroxide nanosheets present are difficult to discern from the Co hydroxide nanoflowers as they closely resemble each other. From the 3D surface render n **Fig. S2f**, the deposit's microstructure is composed of particles of varying sizes spread out across the substrate surface with good adhesion. The deposit appears to be mainly 8.4 μm thick, which is the same as that of unary Co hydroxide, possibly due to the high percentage of Co hydroxide present.

3.3.1. Optimisation of ternary metal hydroxide catalyst

Since the Ni-Fe-Co ternary metal hydroxide catalyst demonstrated the lowest overpotentials at both 0.1 and 0.5 A cm^{-2}, it is selected for further study of the effects of electrodeposition conditions on catalytic performance for OER. The parameters investigated include current density for cathodic deposition, deposition time, pH and temperature of electrolyte solution.

Electrodeposition current density: The effect of cathodic current density on deposit morphology was observed with SEM. The micrograph of the sample deposited at 0.1 A cm^{-2} (**Fig. S6a**) displays particles which are relatively uniform in size and approximately 20-40 μm in characteristic length. Increasing the deposition current density to 0.2 or 0.3 A cm^{-2} results in a faster nucleation rate due to the higher overpotential of the deposition reaction. At a higher current density of 0.5 A cm^{-2} (**Fig. S6b**), the rate of growth of the deposit becomes mass-transfer controlled [71] resulting in larger clusters mixed with small particles of deposit, and the influence of other electrochemical reactions such as hydrogen evolution becomes more prominent. At higher current densities, the deposit particles are larger because of increasing nucleation rate and there are voids in the particles, which are created by the competing

hydrogen evolution reaction. Based on the slow scan voltammogram results, a deposition current density of 0.3 A cm^{-2} gives the best OER catalytic activity for Ni-Fe-Co hydroxide catalyst (**Fig. 8a**). This reduction in OER overpotential at 0.3 A cm^{-2} is due to increased electrocatalytically active surface area from the mixture of large and small deposit particles and voids from hydrogen evolution.

Electrolyte pH: The effect of the deposition solution pH on deposits was investigated by adjusting the solution pH with diluted H_2SO_4 or NaOH. The pH of the unadjusted solution for Ni-Fe-Co hydroxide was approx. 5.5. Since the Fe^{2+} present in the solutions oxidises and precipitates out as insoluble Fe^{3+} at pH > 7.0, the pH of the deposition solution was only adjusted to values in the range of pH 2.5 to 6.6 to avoid precipitation. From the slow scan voltammograms (**Fig. 8b**), it can be seen that OER catalysis increases in the order pH 2.5 < 6.6 < 5.5 < 3.9. This is because at a lower pH, the competing hydrogen evolution reaction is enhanced [72, 73] resulting in weak and unstable deposits which negatively affect catalytic activity for OER. At higher pH values of 3.9 and 5.5, the deposit is more active for OER. Comparing the surface morphology of the deposits at pH 2.5 and 3.9 from SEM micrographs (**Fig. S6c** & **d**), the surface of the deposit from pH 3.9 exhibits porous structures which likely creates more active sites for OER and thus results in higher catalytic activity.

Electrodeposition time: The effect of electrodeposition times between 60 s and 300 s was investigated. At a deposition time of 60 s, the surface of the electrode substrate is more evenly covered by deposit. As the length of electrodeposition time increases, the clusters remain similar in size although some appeared more distorted due to the higher number of voids created by the consistent production of hydrogen bubbles over a prolonged period of time [74-76], which also contributed to the surface of the electrode being less well covered. A deposition time of 240 s was found to give the lowest overpotential value of 235 mV at 0.1 Acm^{-2} for the Ni-Fe-Co hydroxide catalyst (**Fig. 8c**).

Electrodeposition temperature: Distinct morphological changes are observed in the deposits as the electrodeposition temperature is increased. Initially increasing the temperature from 295 K to 308 K, causes the rate of deposition to speed up because of the quicker diffusion of ions and lower nucleation activation energy, resulting in larger deposits forming on the surface of the electrode. At ≥ 323 K, however, the effect of increasing electrodeposition temperature changes abruptly and the structures deposited are thinner, weaker and less compact. Finally, at 343 K, the deposits curl up to expose more uncovered electrode surface as seen in **Fig. S6f**. This can be partially attributed to the enhancement of the rate of hydrogen evolution at the electrode surface as well. Increasing the temperature also leads to observable chemical changes in the electrodeposition sulphate solution which could have had an effect on the electrodeposition reactions. For instance, at ≥ 308 K, insoluble reddish-brown $Fe(OH)_3$ was observed to precipitate out of the Ni-Fe-Co sulphate solution after electrodeposition. Therefore, from **Fig. 8d** the OER overpotential is observed to increase with deposition temperature, with the catalyst prepared at 295 K displaying the lowest overpotential for OER.

Prepared with optimal deposition conditions, the ternary Ni-Fe-Co hydroxide catalyst coated SS mesh and binary 75%Ni 25% Fe hydroxide catalyst coated SS mesh were tested under similar conditions in a three electrode half-cell set-up in comparison with a commercial Ir-Ru mixed oxide coated expanded Ti mesh (**Fig. 8e**). Both binary Ni-Fe and ternary Ni-Fe-Co non-precious metal catalyst coated electrodes show considerable reductions in OER overpotential, illustrating better performance compared to the precious metal oxide catalyst coated electrode.

3.3.2 Further characterisation of optimised ternary metal hydroxide catalyst

The optimised Ni-Fe-Co ternary hydroxide catalyst was deposited onto a carbon polymer plate and examined with SEM, EDX and XPS before and after undergoing OER at a current

density of 0.1 A cm^{-2} for 15 mins. From the SEM images of the catalyst surface before (**Fig. S6g**) and after OER (**Fig. S6h**), it is clear that the surface becomes rougher and more porous after OER. EDX analysis of the surface revealed that the atomic composition of the deposit remained fairly constant across the electrode before and after oxygen evolution, confirming sample homogeneity.

XPS spectra of the ternary Ni-Fe-Co hydroxide before and after OER display changes that occur during the surface chemical reactions. In the Co2p spectra of the sample before OER (**Fig. 9a**), the peak at 781.3 eV with accompanying satellite peak at 786.2 eV confirms the presence of $Co(OH)_2$. After the sample was subjected to oxidising conditions, the Co2p spectra displays a $Co2p_{3/2}$ peak at binding energy 780.4 eV which is characteristic of $Co^{3+/4+}$ in both CoOOH and Co_3O_4 due to their slightly overlapping binding energies. Given the absence of the accompanying satellite peak of the $Co2p_{3/2}$ peak at 786.2 eV as well, it is apparent that the Co^{3+} species is present predominantly as CoOOH [60, 63]. In addition to this, the difference in binding energy of multiplet peaks $2p_{3/2}$ and $2p_{1/2}$ peaks before evolving oxygen is ≈16 eV which is characteristic of $Co(OH)_2$ and after evolving oxygen it is reduced to ≈15 eV which is characteristic of CoOOH [77] (**Fig. 9b**). It is therefore evident that during the evolution of oxygen, reaction (10) takes place.

$$Co(OH)_2 + OH^- \rightarrow CoOOH + H_2O + e^- \qquad (10)$$

The $Ni2p_{3/2}$ spectra (**Fig. 9c**) for the sample before OER displays a peak at 856.4 eV and corresponding satellite peak at 861.2 eV characteristic of $Ni(OH)_2$ as described earlier. However, after evolving oxygen the binding energies of the $2p_{3/2}$ and $2p_{1/2}$ peaks are shifted to slightly lower values which are characteristic of Ni^{3+} in NiOOH and the corresponding satellite peaks also appear broader and flattened [50, 78]. This suggests that under OER conditions the $Ni(OH)_2$ also undergoes oxidation to form NiOOH, reaction (1).

Due to the extremely low quantity of Fe species present in the surface of the deposit, the

Fe $2p_{3/2}$ and $2p_{1/2}$ peaks are not well defined as shown in **Fig. 9d**. Comparing the electron binding energies before and after OER, the $Fe2p_{3/2}$ peak at 712.7 eV, which is characteristic of Fe^{3+}, did not change significantly. The observation that Fe remains in the 3^+ oxidation state after OER was also seen in other detailed studies on Fe-incorporated oxide and oxyhydroxide catalysts [35, 64, 70]. For a similar ternary Ni-Fe-Co metal oxide catalyst, it was proposed that the presence of Ni and Co activated the Fe active sites for binding to OER intermediates –OH and –OOH, leading to enhanced OER activity compared to the binary Ni-Fe oxide [70].

The O1s spectra of the Ni-Fe-Co ternary metal hydroxide before OER in **Fig. 9e** shows a peak at 532.0 eV which is characteristic of the M-OH bond in $Ni(OH)_2$ and $Co(OH)_2$, and a peak at 531.2 eV which can be assigned to the O^{2-} and OH^- oxygen atoms in FeOOH [53]. After evolving oxygen, the O1s spectra reveals a decrease in signal area for the peak at 532.0 eV due to the oxidation of $Ni(OH)_2$ and $Co(OH)_2$ to NiOOH and CoOOH respectively. Correspondingly, the peak at 531.2 eV increases in signal area after OER which is attributed to the presence of the M-OH bond for CoOOH [63] and M-O bond for NiOOH [79], and a small peak at 529.8 eV in the O1s spectra after OER is assigned to the M-O bond in CoOOH [63]. Lastly, a minor peak at 535.9 eV was observed in the O1s spectra after OER and assigned to gaseous phase H_2O [80]. These observations are in good agreement with the other spectra.

3.4. Stability tests in an AEM water electrolyser cell

Preliminary stability tests of binary 75%Ni 25%Fe metal hydroxide and the optimised Ni-Fe-Co ternary metal hydroxide were carried out in an alkaline zero-gap water electrolyser with a working area of 9 cm^2. The current density was held at 0.5 A cm^{-2} for a period of 3.5 hours and the cell voltage was recorded during this time.

The cell voltage, E_{cell}, of an AEM electrolyser is given by the equation

$$-E_{cell} = \Delta E_e - |\eta_a| - |\eta_c| - IR \qquad (11)$$

Where ΔE_e is the difference in equilibrium potentials for the two electrode reactions, i.e. -1.23 V (at 298 K, 1 atm), η are the overpotentials at anode and cathode respectively, I is the cell current and R is resistance. In order to achieve a higher cell efficiency, E_{cell} needs to be minimised. The minimisation of the overpotentials is dependent on the availability of efficient electrocatalysts whilst the minimisation of the IR term is dependent on good engineering design. Plots of cell voltage, E_{cell}, against time for the AEM electrolyser assembled with uncoated and catalyst-coated SS anodes are shown in **Fig. 10**. The E_{cell} of the electrolyser assembled with uncoated SS mesh anode was found to be 2.33 V. In comparison, the E_{cell} of the electrolyser assembled with anodes of Ni-Fe binary hydroxide coated SS mesh is 2.26 V (or 70 mV reduction in E_{cell}) and with Ni-Fe-Co ternary hydroxide catalyst is 2.22 V (or 110 mV reduction). As the cells were assembled with the same cathode material, and operated under the same conditions, the reductions in overall cell voltage are brought about by the Ni-Fe binary hydroxide and Ni-Fe-Co ternary hydroxide catalyst coatings. Also the voltages of these cells were demonstrated to be very stable during the testing period. Therefore, in this study, the test results have shown that the Ni-Fe-Co hydroxide catalyst is more effective at reducing the OER overpotential which contributes significantly to a higher cell efficiency.

4. Conclusion

Ni-based binary and ternary metal hydroxide catalysts were prepared using a cathodic electrodeposition method from metal sulphate solutions. The compositions of Ni-based binary metal hydroxide catalysts Ni-Fe, Ni-Co, Ni-Mo and NiCr were initially optimised and the composition of Ni-Fe based ternary metal hydroxide catalysts were later derived from the optimal binary Ni-Fe and Ni-Co, Ni-Mo and Ni-Cr metal hydroxide catalyst compositions. Ternary metal hydroxide catalysts Ni-Fe-Co and Ni-Fe-Mo, which were also synthesised by cathodic electrodeposition, showed significantly lower overpotentials for oxygen evolution

compared to their binary and unary metal hydroxide counterparts.

The influence of electrodeposition parameters on the synthesis of ternary Ni-Fe-Co hydroxide catalyst films and their effect on the catalytic performance were investigated. It was found that the catalyst cathodically deposited at 0.3 A cm^{-2} for 240 s at 295 K in a pH 3.9 electrodeposition solution produced the most active catalyst with an overpotential value of 235 mV at 0.1 A cm^{-2} when tested in 1 M NaOH, 333 K. The catalytic activity of the optimised Ni-Fe-Co ternary hydroxide catalyst was proven to be better than Ni-Fe binary hydroxide and uncoated SS mesh when tested in an alkaline zero-gap electrolyser at 0.5 A cm^{-2} for 3.5 h giving a potential of 2.22 V.

Conflicts of interest

There are no conflicts to declare.

Acknowledgements

Adeline Loh would like to acknowledge the PhD studentship awarded by the College of Engineering, Mathematics and Physical Sciences in the University of Exeter. Funding: This work was partly supported by the EPSRC Supergen Energy Storage Project (grant number: EP/P003494/1) entitled ‘Zinc-Nickel Redox Flow Battery for Energy Storage’; the European Interreg 2 Seas programme 2014- 2020 co-funded by the European Regional Development Fund under subsidy contract No [2S03-019].

References

1. O.Schmidt, A.Gambhir, I.Staffell, A.Hawkes, J.Nelson, S.Few, Future cost and performance of water electrolysis: An expert elicitation study, Int. J. Hydrogen Energy 42 (2017) 30470-92.
2. V. T.N., Hydrogen Energy, Springer, Boston, MA, 1975
3. M. Carmo, D. L.Fritz, J. Mergel, D. Stolten, A comprehensive review on PEM water electrolysis, Int. J. Hydrogen Energy 38 (2013) 4901-34.
4. D. Pletcher, X. Li, Prospects for alkaline zero gap water electrolysers for hydrogen production, Int. J. Hydrogen Energy 36 (2011) 15089-104.
5. A.I. Krasil'shckov, On the intermediate stages of anodic oxygen evolution., Zh. Fiz. Khim. 37 (1963) 273.
6. J.O.M. Bockris, Kinetics of activation controlled consecutive electrochemical reactions: anodic evolution of oxygen, J. Chem. Phys. 24 (1956) 817.
7. F. Lu, M. Zhou, Y. Zhou, X. Zeng, First-row transition metal based catalysts for the oxygen evolution reaction under alkaline conditions: basic principles and recent advances, Small 13 (2017) 1701931.
8. S. Matsumoto, Electrocatalytic properties of transition metal oxides for oxygen evolution reaction, Mater. Chem. Phys. 14 (1986) 397-426.
9. F. Lu, M. Zhou, Y. Zhou, X. Zeng, First-row transition metal based catalysts for the oxygen evolution reaction under alkaline conditions: basic principles and recent advances, Small 13 (2017) 1-18.
10. M.E.G. Lyons, M.P. Brandon, The oxygen evolution reaction on passive oxide covered transition metal electrodes in aqueous alkaline solution. Part 1-Nickel, Int. J. Electrochem. Sci 3 (2008) 1386-424.
11. M.E.G. Lyons, M.P. Brandon, The oxygen evolution reaction on passive oxide covered transition metal electrodes in alkaline solution. Part II - Cobalt, Int. J. Electrochem. Sci 3 (2008) 1425-62.
12. M.E.G. Lyons, M.P. Brandon, The oxygen evolution reaction on passive oxide covered transition metal electrodes in alkaline solution. Part III – Iron., Int. J. Electrochem. Sci 3 (2008) 1463-503.
13. M.S. Burke, S. Zou, L.J. Enman, J.E. Kellon, C.A. Gabor, E. Pledger, S.W. Boettcher, Revised oxygen evolution reaction activity trends for first-row transition-metal (oxy)hydroxides in alkaline media, Phys. Chem. Lett. 6 (2015) 3737-42.
14. D.T. Ram Subbaraman, Kee-Chul Chang, Dusan Strmcnik, Arvydas P. Paulikas, Pussana Hirunsit, Maria Chan, Jeff Greeley, Vojislav Stamenkovic, Nenad M. Markovic, Trends in activity for the water electrolyser reactions on 3d M(Ni, Co, Fe, Mn) hydr(oxy)oxide catalysts, Nat. Mater. 11 (2012) 550-557.
15. L. Trotochaud, J.K. Ranney, K.N. Williams, S.W. Boettcher, Solution-Cast Metal Oxide Thin Film Electrocatalysts for Oxygen Evolution, J. Am. Chem. Soc. 134 (2012) 17253-17261.
16. M.E.G. Lyons, M.P. Brandon, A comparative study of the oxygen evolution reaction on oxidised nickel, cobalt and iron electrodes in base, J. Electroanal. Chem. 641 (2010) 119-30.
17. Xiaohong Li, Frank C. Walsh, D. Pletcher, Nickel based electrocatalysts for oxygen evolution in high current density, alkaline water electrolysers, Phys. Chem. Chem. Phys. 13 (2010) 1162-7.
18. P. Olivia, J. Leonardi, J.F. Laurent, C. Delmas, J.J. Braconnier, M. Figlarz, F. Fievet, A.d. Guibert, Review of the structure and the electrochemistry of nickel hydroxides and oxy-hydroxides, J. Power Sources 8 (1982) 229-55.
19. O. Diaz-Morales, I. Ledezma-Yanez, M.T.M. Koper, F. Calle-Vallejo, Guidelines for the rational design of Ni-based double hydroxide electrocatalysts for the oxygen evolution reaction, ACS Catal. 5 (2015) 5380-7.
20. P. Wang, Y. Lin, L. Wan, B. Wang, Autologous growth of Fe-doped Ni(OH)2 nanosheets with low overpotential for oxygen evolution reaction, Int. J. Hydrogen Energy 45 (2020) 6416-24.
21. S.L. Suib, New and Future Developments in Catalysis: Hybrid Materials, Composites, and Organocatalysts. 2013, Newnes: Elsevier
22. M.M. Jaksic, Interionic nature of synergism in catalysis and electrocatalysis, Solid State Ion. 136-137 (2000) 733-46.
23. S.I. Cordoba, R.E. Carbonio, M.L. Teijelo, V.A. Macagno, The electrochemical response of binary mixtures of hydrous transition metal hydroxides co-precipitated on conducting substrates with reference to the oxygen evolution reaction, Electrochim. Acta 31 (1986) 1321-1332.
24. D.A. Corrigan, The catalysis of the oxygen evolution reaction by iron impurities in thin film nickel oxide electrodes, J. Electrochem. Soc. 134 (1987) 377-384.
25. M.B. Stevens, L.J. Enman, E.H. Korkus, J. Zaffran, C.D.M. Trang, J. Asbury, M.G. Kast, M.C. Toroker, S.W. Boettcher, Ternary Ni-Co-Fe oxyhydroxide oxygen evolution catalysts: Intrinsic activity trends, electrical conductivity, and electronic band structure, Nano Res. 12 (2019) 2288-95.
26. James B. Gerken, Sarah E. Shaner, Robert C. Mass´e, Nicholas J. Porubsky, S.S. Stahl, A survey of diverse earth abundant oxygen evolution electrocatalysts showing enhanced activity from Ni–Fe oxides

containing a third metal, Energy Environ. Sci. 7 (2014) 2376-2382.
27. Jamie Y. C. Chen, Jeffrey T. Miller, James B. Gerken, S.S. Stahl, Inverse spinel NiFeAlO4 as a highly active oxygen evolution electrocatalyst: Promotion of activity by a redox-inert metal ion, Energy Environ. Sci. 7 (2014) 1382-1386.
28. X. Bo, Y. Li, R.K. Hocking, C. Zhao, NiFeCr hydroxide holey nanosheet as advanced electrocatalyst for water oxidation, ACS Appl. Mater. Interfaces 9 (2017) 41239-45.
29. Y. Jin, S. Huang, X. Yue, H. Du, P.K. Shen, Mo- and Fe-modified Ni(OH)2/NiOOH nanosheets as highly active and stable electrocatalysts for oxygen evolution reaction, ACS Catal. 8 (2018) 2359-63.
30. K.N. Dinh, P. Zheng, Z. Dai, Y. Zhang, R. Dangol, Y. Zheng, B. Li, Y. Zong, Q. Yan, Ultrathin porous NiFeV ternary layer hydroxide nanosheets as a highly efficient bifunctional electrocatalyst for overall water splitting, Small 14 (2018) 1703257.
31. R.N. Singh, J.P. Singh, B. Lala, M.J.K. Thomas, S. Bera, New NiFe2−xCrxO4 spinel films for O2 evolution in alkaline solutions, Electrochim. Acta 51 (2006) 5515-5523.
32. F.J. Perez-Alonso, C. Adan, S. Rojas, M.A. Pena, J.L.G. Fierro, Ni/Fe electrodes prepared by electrodeposition method over different substrates for oxygen evolution reaction in alkaline medium, Int. J. Hydrogen Energy 39 (2014) 5204-5212.
33. K. Sardar, S.C. Ball, J.D.B. Sharman, D. Thompsett, J.M. Fisher, R.A.P. Smith, P.K. Biswas, M.R. Lees, R.J. Kashtiban, J. Sloan, R.I. Walton, Bismuth iridium oxide oxygen evolution catalyst from hydrothermal synthesis, Chem. Mater. 24 (2012) 4192-200.
34. C. Iwakura, A. Honji, H. Tamura, The anodic evolution of oxygen on Co3O4 film electrodes in alkaline solutions, Electrochim. Acta 26 (1981) 1319-26.
35. M. Gong, Y. Li, H. Wang, Y. Liang, J.Z. Wu, J. Zhou, J. Wang, T. Regier, F. Wei, H. Dai, An advanced Ni−Fe layered double hydroxide electrocatalyst for water oxidation, J. Am. Chem. Soc. 135 (2013) 8452-5.
36. A.V. Naumkin, A. Kraut-Vass, S.W. Gaarenstroom, C.J. Powell. *NIST X-ray Photoelectron Spectroscopy Database* 2012 15/09/2012 [cited 2018; Version 4.1 [Available from: http://srdata.nist.gov/xps/.
37. J. Eigeldinger, H. Vogt, The bubble coverage of gas-evolving electrodes in a flowing electrolyte, Electrochim. Acta 45 (2000) 4449-56.
38. Debabrata Chanda, Jaromir Hnat, Martin Paidar, K. Bouzek, Evolution of physicochemical and electrocatalytic properties of NiCo2O4 (AB2O4) spinel oxide with the effect of Fe substitution at the A site leading to efficient anodic O2 evolution in an alkaline environment, Int. J. Hydrogen Energy 39 (2014) 5713-22.
39. A. Damjanovic, A.Dey, J.O.M. Bockris, Kinetics of oxygen evolution and dissolution on platinum electrodes, Electrochim. Acta 11 (1966) 791-814.
40. N.-T. Suen, S.-F. Hung, Q. Quan, N. Zhang, Y.-J. Xu, H.M. Chen, Electrocatalysis for the oxygen evolution reaction: recent development and future perspectives, Chem. Soc. Rev. 46 (2017) 337-65.
41. A.Damjanovic, A.Dey, J.O'M.Bockris, Kinetics of oxygen evolution and dissolution of platinum electrodes, Electrochim. Acta 11 (1966) 791-814.
42. S. Trasatti, Electrodes of Conductive Metallic Oxides Part B, Elsevier, Amsterdam, 1981
43. D.S. Hall, D.J. Lockwood, C. Bock, B.R. MacDougall, Nickel hydroxides and related materials: a review of their structures, synthesis and properties, Pro. R. Soc. A 471 (2014) 1-65.
44. D. Hunt, G. Garbarino, J.A. Rodríguez-Velamazán, V. Ferrari, M. Jobbagy, D.A. Scherlis, The magnetic structure of β-cobalt hydroxide and the effect of spin-orientation, Phys. Chem. Chem. Phys. 18 (2016) 30407-14.
45. V.Yu.Kazimirov, M.B.Smirnov, L.Bourgeois, L.Guerlou-Demourgues, L.Servant, A.M.Balagurov, I.Natkaniec, N.R.Khasanova, E.V.Antipov, Atomic structure and lattice dynamics of Ni and Mg hydroxides, Solid State Ionics 181 (2010) 1764-70.
46. I. Lozano, N. Casillas, C.P.d. León, F.C. Walsh, P. Herrasti, New insights into the electrochemical formation of magnetite nanoparticles, J. Electrochem. Soc. 164 (2017) D184-91.
47. E.R. Encina, M. Distaso, R.N.K. Taylor, W. Peukert, Synthesis of goethite α-FeOOH particles by air oxidation of ferrous hydroxide Fe(OH)2 suspensions: Insight on the formation mechanism, Cryst. Growth Des. 15 (2015) 194-203.
48. A.M. Venezia, R. Bertoncello, G. Deganello, X-ray photoelectron spectroscopy investigation of pumice-supported nickel catalysts Surf. Interface Anal. 23 (1995) 239-47.
49. B.P. Payne, M.C. Biesinger, N.S. McIntyre, Use of oxygen/nickel ratios in the XPS characterisation of oxide phases on nickel metal and nickel alloy surfaces, J. Electron. Spectrosc. Relat. Phenom. 185 (2012) 159-66.
50. A.P. Grosvenor, M.C. Biesinger, R.S.C. Smart, N.S. McIntyre, New interpretations of XPS spectra of nickel metal and oxides, Surf. Sci. 600 (2006) 1771-9.

51. M.C. Biesinger, B.P. Payne, L.W.M. Lau, A. Gerson, R.S.C. Smart, X-ray photoelectron spectroscopic chemical state quantification of mixed nickel metal, oxide and hydroxide systems, Surf. Interface Anal. 41 (2008) 324-32.
52. H.W. Nesbitt, D. Legrand, G.M. Bancroft, Interpretation of Ni2p XPS spectra of Ni conductors and Ni insulators, Phys. Chem. Min. 27 (2000) 357-66.
53. G.C. Allen, M.T. Curtis, A.J. Hooper, P.M. Tucker, X-ray photoelectron spectroscopy of iron-oxygen systems JCS. Dalton 14 (1974) 1525-30.
54. P.C.J. Graat, M.A.J. Somers, Simultaneous determination of composition and thickness of thin iron-oxide films from XPS Fe 2p spectra Appl. Surf. Sci. 100 (1996) 36-40.
55. M. Descostes, F. Mercier, N. Thromat, C.Beaucairea, M.Gautier-Soyer, Use of XPS in the determination of chemical environment and oxidation state of iron and sulfur samples: constitution of a data basis in binding energies for Fe and S reference compounds and applications to the evidence of surface species of an oxidized pyrite in a carbonate medium, Appl. Surf. Sci. 165 (2000) 288-302.
56. T. Yamashita, P. Hayes, Analysis of XPS spectra of Fe2+ and Fe3+ ions in oxide materials, Appl. Surf. Sci. 254 (2008) 2441-9.
57. N.S. McIntyre, D.G. Zetaruk, X-ray photoelectron spectroscopic studies of iron oxides, Anal. Chem. 49 (1977) 1521-9.
58. A.P. Grosvenor, B.A. Kobe, M.C. Biesinger, N.S. McIntyre, Investigation of multiplet splitting of Fe 2p XPS spectra and bonding in iron compounds, Surf. Interface Anal. 36 (2004) 1564-74.
59. D.C. Frost, C.A. McDowell, L.S. Woolsey, Evidence for multiplet splitting of 2p photoelectron lines of transition metal complexes, Chem. Phys. Lett. 17 (1972) 320-3.
60. N.S. McIntyre, M.G. Cook, X-ray photoelectron studies on some oxides and hydroxides of cobalt, nickel, and copper, Anal. Chem. 47 (1975) 2208-13.
61. D.C. Frost, C.A. McDowell, I.S. Woolsey, X-ray photoelectron spectra of cobalt compounds, Mol. Phys. 27 (1974) 1473-89.
62. M.C. Biesinger, B.P. Payne, A.P. Grosvenor, L.W.M. Lau, A.R. Gerson, R.S.C. Smart, Resolving surface chemical states in XPS analysis of first row transition metals, oxides and hydroxides: Cr, Mn, Fe, Co and Ni, Appl. Surf. Sci. 257 (2011) 2717-30.
63. J. Yang, H. Liu, W.N. Martens, R.L. Frost, Synthesis and characterization of cobalt hydroxide, cobalt oxyhydroxide, and cobalt oxide nanodiscs, J. Phys. Chem. C 114 (2010) 111-19.
64. D. Friebel, M.W. Louie, M. Bajdich, K.E. Sanwald, Y. Cai, A.M. Wise, M.-J. Cheng, D. Sokaras, T.-C. Weng, R. Alonso-Mori, R.C. Davis, J.R. Bargar, J.K. Nørskov, A. Nilsson, A.T. Bell, Identification of highly active Fe sites in (Ni,Fe)OOH for electrocatalytic water splitting, J. Am. Chem. Soc. 137 (2015) 1305-1313.
65. Lena Trotochaud, Samantha L. Young, James K. Ranney, S.W. Boettcher, Nickel−iron oxyhydroxide oxygen-evolution electrocatalysts: the role of intentional and incidental iron incorporation, J. Am. Chem. Soc. 136 (2014) 6744-53.
66. S.J. Charles C. L. McCrory, Jonas C. Peters and Thomas F. Jaramillo, Benchmarking heterogeneous electrocatalysts for the oxygen evolution reaction, J. Am. Chem. Soc. 135 (2013) 16977−87.
67. K.Y. Sasaki, J.B. Talbot, Electrodeposition of binary iron-group alloys, J. Electrochem. Soc. 142 (1995) 775-82.
68. M.W. Louie, A.T. Bell, An investigation of thin-film Ni–Fe oxide catalysts for the electrochemical evolution of oxygen, J. Am. Chem. Soc. 135 (2013) 12329-37.
69. M. Bajdich, M. García-Mota, A. Vojvodic, J.K. Nørskov, A.T. Bell, Theoretical investigation of the activity of cobalt oxides for the electrochemical oxidation of water, J. Am. Chem. Soc. 135 (2013) 13521-30.
70. M.K. Bates, H.D. Qingying Jia, Wentao Liang, S. Mukerjee, Charge-transfer effects in Ni−Fe and Ni−Fe−Co mixed-metal oxides for the alkaline oxygen evolution reaction, ACS Catal. 6 (2016) 155-61.
71. A.M. Rashidi, A. Amadeh, The effect of current density on the grain size of electrodeposited nanocrystalline nickel coatings, Surf. Coat. Technol. 202 (2008) 3772-76.
72. Y. Yang, Preparation of Fe-Co-Ni ternary alloys with electrodeposition, Int. J. Electrochem. Sci. 10 (2015) 5164-75.
73. J.B. O'Sullivan, Studies in the electro-deposition of nickel. Part I. The effect of pH and of various buffering agents; the presence of oxygen in the deposits, Trans. Faraday Soc. 26 (1930) 89-93.
74. F. Ebrahimi, Z. Ahmed, The effect of current density on properties of electrodeposited nanocrystalline nickel, J. Appl. Electrochem. 33 (2003) 733-9.
75. N.A. Resali, K.M. Hyie, M.N.Berhan, Z. Salleh, S. Kasolang, Cobalt-nickel-iron nanoparticles coated on stainless steel substrate, Procedia Eng. 68 (2013) 30-6.
76. K.-Q. Zhang, M. Wang, R.-W. Peng, Y. Xiao, N.-b. Ming, H3O+-dependent morphological change in the electrochemical deposition of iron, Phys. Lett. A 278 (2001) 286-92.

77. C.V. Schenck, J.G. Dillard, J.W. Murray, Surface analysis and the adsorption of Co(ll) on goethite J. Colloid Interface Sci. 95 (1983) 398-409.
78. H. Sambe, T.M. Nabi, D.E. Ramaker, A.N. Mansour, W.E. O'Grady, *The oxidation state of Ni in the nickel oxide electrode and related nickel oxide compounds: 1. Spectroscopic evidence*. 1997, Office of Naval Research: Arlington, VA.
79. I.G. Casella, M.R. Guascito, M.G. Sannazzaro, Voltammetric and XPS investigations of nickel hydroxide electrochemically dispersed on gold surface electrodes, J. Electroanal. Chem. 462 (1999) 202-10.
80. H. Ali-Löytty, M.W. Louie, M.R. Singh, L. Li, H.G.S. Casalongue, H. Ogasawara, E.J. Crumlin, Z. Liu, A.T. Bell, A. Nilsson, D. Friebel, Ambient-pressure XPS study of a Ni−Fe electrocatalyst for the oxygen evolution reaction, J. Phys. Chem. C 120 (2016) 2247-53.

Table 1 Overpotentials of OER and Tafel slope values for unary Ni, Fe, Co, Mo and Cr and binary Ni-Fe, Ni-Co, Ni-Mo and Ni-Cr hydroxides tested in 1 M NaOH, 333 K.

Binary hydroxide	Electrodeposition bath composition/ molar %	Overpotential of OER, $\eta_{0.5\ A\ cm^{-2}}$ / mV	Overpotential of OER, $\eta_{0.1\ A\ cm^{-2}}$ / mV	Tafel slope, *b* / mV dec^{-1}
Ni-Fe	100:0	348	307	40
	75:25	**323**	**292**	**48**
	50:50	341	304	39
	25:75	354	320	42
	0:100	400	357	42
Ni-Co	75:25	332	299	36
	50:50	326	298	34
	25:75	**322**	**295**	**36**
	0:100	335	301	38
Ni-Mo	75:25	357	312	41
	50:50	**335**	**298**	**42**
	25:75	339	300	42
	0:100	420	361	50
Ni-Cr	**75:25**	**329**	**293**	**38**
	50:50	354	309	43
	25:75	379	333	44
	0:100	387	337	43

Table 2 Overpotentials of OER and Tafel slope values for Ni-Fe based ternary metal hydroxide catalysts tested in 1 M NaOH, 333 K.

Ternary hydroxide	Electrodeposition bath composition/ molar %	Electrodeposition conditions	Overpotential of OER, $\eta_{0.5\ A\ cm^{-2}}$ / mV	Overpotential of OER, $\eta_{0.1\ A\ cm^{-2}}$ / mV	Tafel slope, *b* / mV dec^{-1}
Ni-Fe-Cr	**75:12.5:12.5**	0.2 A cm^{-2} for 120 s at 22 ºC	**322**	**287**	48
	70:20:10		339	301	53
	66:17:17		335	299	46
Ni-Fe-Mo	**44.5:11:44.5**		**300**	**270**	**40**
	62.5:12.5:25		319	282	44
	40:10:50		309	279	37
Ni-Fe-Co	62.5:12.5:25		326	296	40
	44.5:11:44.5		316	290	31
	23:8:69		**296**	**265**	**37**
	23:8:69	0.3 A cm^{-2} for 240 s at 22 ºC, pH adjusted to 3.9	**262**	**235**	**36**

Figure Captions

Fig. 1 Cyclic voltammograms of cathodically electrodeposited $Ni(OH)_2$ on the surface of the SS microelectrode at 0.2 A cm^{-2} for 120 s from 18 mM $NiSO_4.6H_2O$ + 25 mM $(NH_4)_2SO_4$ solution. The sample was cycled between 0.1 and 0.7 V *vs.* Hg/ HgO in 1 M NaOH, 333 K at 100 mV s^{-1}.

Fig. 2 a) Cyclic voltammograms swept at 100 mV s^{-1} between 0.1 and 0.7 V, **b)** linear sweep voltammograms swept at 1 mV s^{-1} from 0.45 to 0.75 V, and **c)** Tafel slope plots of unary Ni, Fe, Co, Mo and Cr hydroxide catalysts tested in 1 M NaOH, 333 K. All catalysts were cathodically electrodeposited at 0.2 A cm^{-2} for 120 s onto the surface of the SS microelectrode from their respective 18 mM metal sulphate + 25 mM $(NH_4)_2SO_4$ solutions.

Fig. 3 i) SEM micrographs **ii)** TEM micrographs and **iii)** corresponding diffraction patterns of cathodic depositions from 18 mM **a)** Ni **b)** Fe and **c)** Co sulphate, + 25 mM $(NH_4)_2SO_4$ solutions.

Fig. 4 XPS M-2p spectra for samples cathodically deposited at 0.2 A cm^{-2} for 120 s from their respective 18 mM sulphate solutions of **a)** Ni **b)** Fe and **c)** Co and the combined **d)** O1s spectra of these samples. All sulphate solutions contained 25 mM $(NH_4)_2SO_4$.

Fig. 5 a) Cyclic voltammograms cycled at 100 mV s^{-1} between 0.1 and 0.7 V, **b)** linear sweep voltammograms swept at 1 mV s^{-1} from 0.45 to 0.75 V and **c)** Tafel slope plots of Ni-Fe binary hydroxide catalysts tested in 1 M NaOH, 333 K. All catalysts were cathodically electrodeposited at 0.2 A cm^{-2} for 120 s onto the surface of the SS microelectrode from their respective metal sulphate solutions.

Fig. 6 TEM images of cathodic depositions at 200 mA cm^{-2} for 120 s from 18 mM metal sulphate solutions of **a)** 75% Ni 25% Fe **b)** 25% Ni 75% Co and **c**) 23% Ni 8% Fe 69% Co. All sulphate solutions contained 25 mM $(NH_4)_2SO_4$.

Fig. 7 Steady state polarisation curves swept at 1 mV s^{-1} from 0.45 to 0.75 V in 1 M NaOH, 333 K for various unary, binary and ternary catalysts cathodically deposited at 0.2 A cm^{-2} for 120 s at 295 K on the SS microelectrode from their respective 18 mM metal sulphate solutions.

Fig. 8 Steady state polarisation curves of Ni-Fe-Co ternary hydroxide catalysts prepared from 18 mM metal sulphate solution of 23%Ni-8%Fe-69%Co + 25 mM $(NH_4)_2SO_4$ at different **a)**

cathodic current densities **b)** pH **c)** electrodeposition times and **d)** electrodeposition temperatures. All catalyst samples were swept at 1 mV s^{-1} from 0.45 to 0.75 V in 1 M NaOH, 333 K. **e)** Comparison of OER performance of the optimised Ni-Fe-Co hydroxide catalyst coated electrode to benchmark commercial electrode at 20 mA cm^{-2} in 4 M NaOH, 333 K.

Fig. 9 XPS **a)** $Co2p_{3/2}$ **b)** Co2p **c)** Ni2p **d)** Fe2p **e)** O1s spectra of the optimised Ni-Fe-Co ternary hydroxide catalyst before and after being held at 0.1 A cm^{-2} for 15 mins.

Fig. 10 Cell voltages, E_{cell}, of zero-gap alkaline water electrolyser assembled with uncoated and catalyst coated SS anodes and expanded Ni mesh cathode pressed up against Tokuyama A201 hydroxide ion exchange membrane held at 0.5 A cm^{-2} for a period of 3.5 h in 4 M NaOH at 333 K and 250 mL min^{-1} electrolyte pump rate.

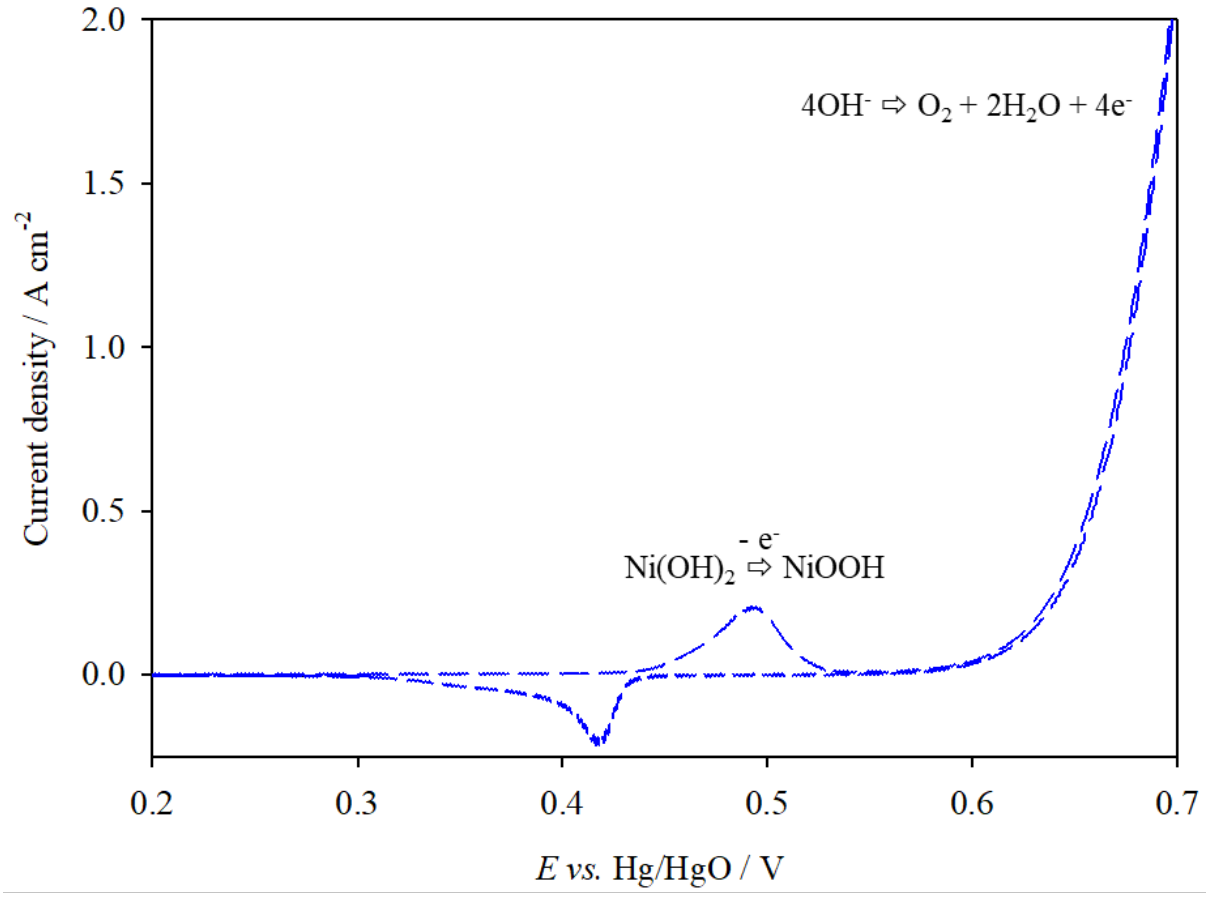
2.0
1.5
1.0
0.5
0.0
Current density / A cm-2
4OH- ⇨ O2 + 2H2O + 4e-
- e-
Ni(OH)2 ⇨ NiOOH
0.2
0.3
0.4
0.5
0.6
0.7
E vs. Hg/HgO / V

Fig. 1

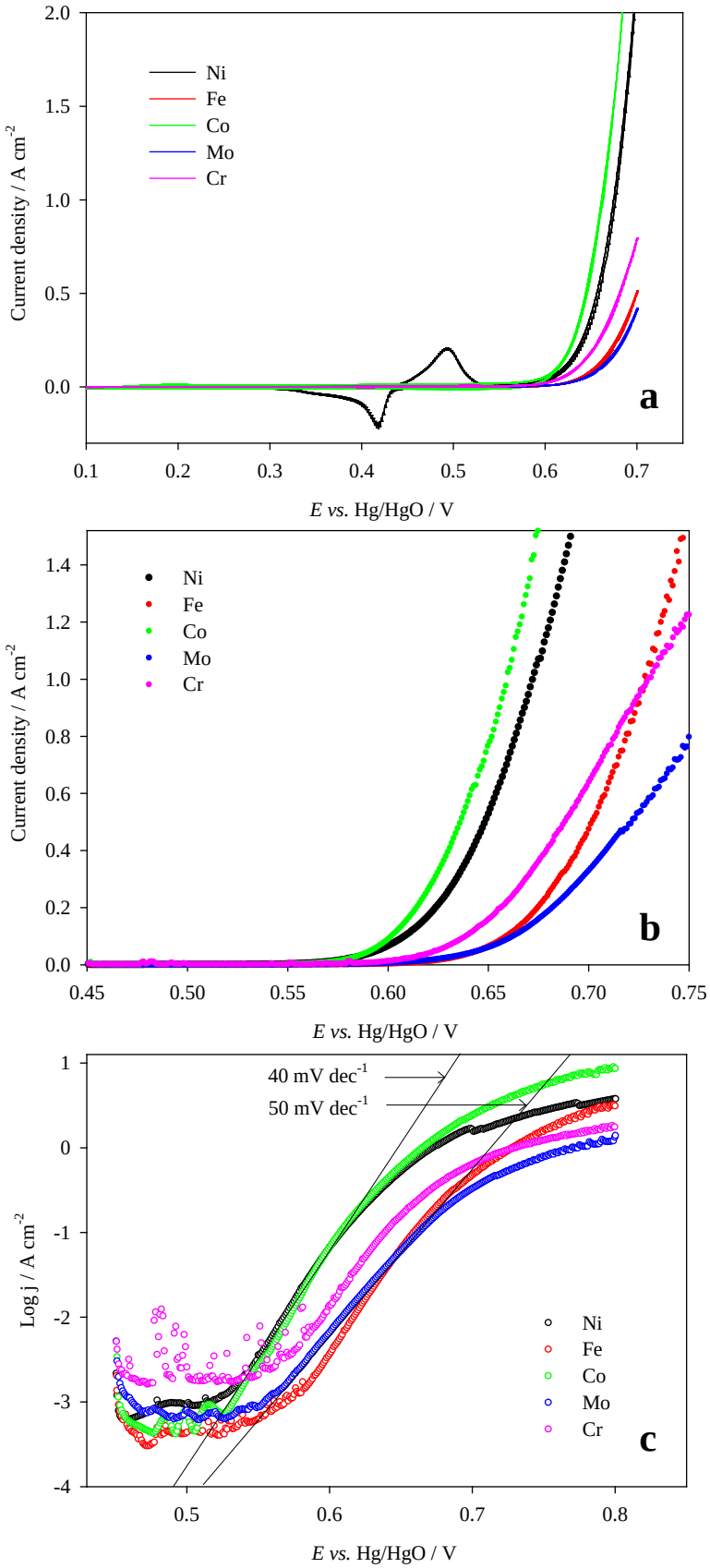
Ni
Fe
Co
Mo
Cr
Current density / A cm-2
E vs. Hg/HgO / V
a
b
40 mV dec-1
50 mV dec-1
Log j / A cm-2
c

Fig. 2

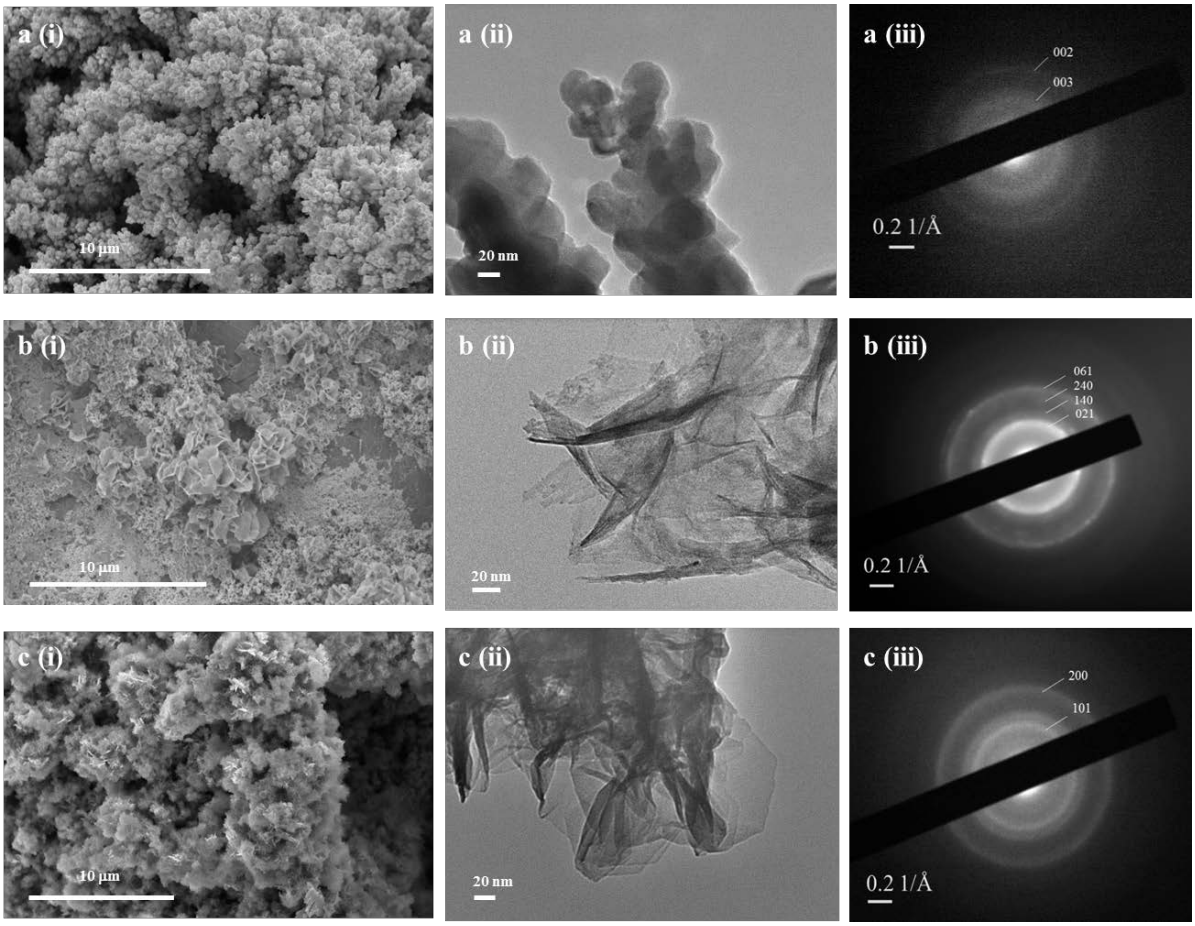
a (i)
10 µm
a (ii)
20 nm
a (iii)
002
003
0.2 1/Å
b (i)
10 µm
b (ii)
20 nm
b (iii)
061
240
140
021
0.2 1/Å
c (i)
10 µm
c (ii)
20 nm
c (iii)
200
101
0.2 1/Å

Fig. 3

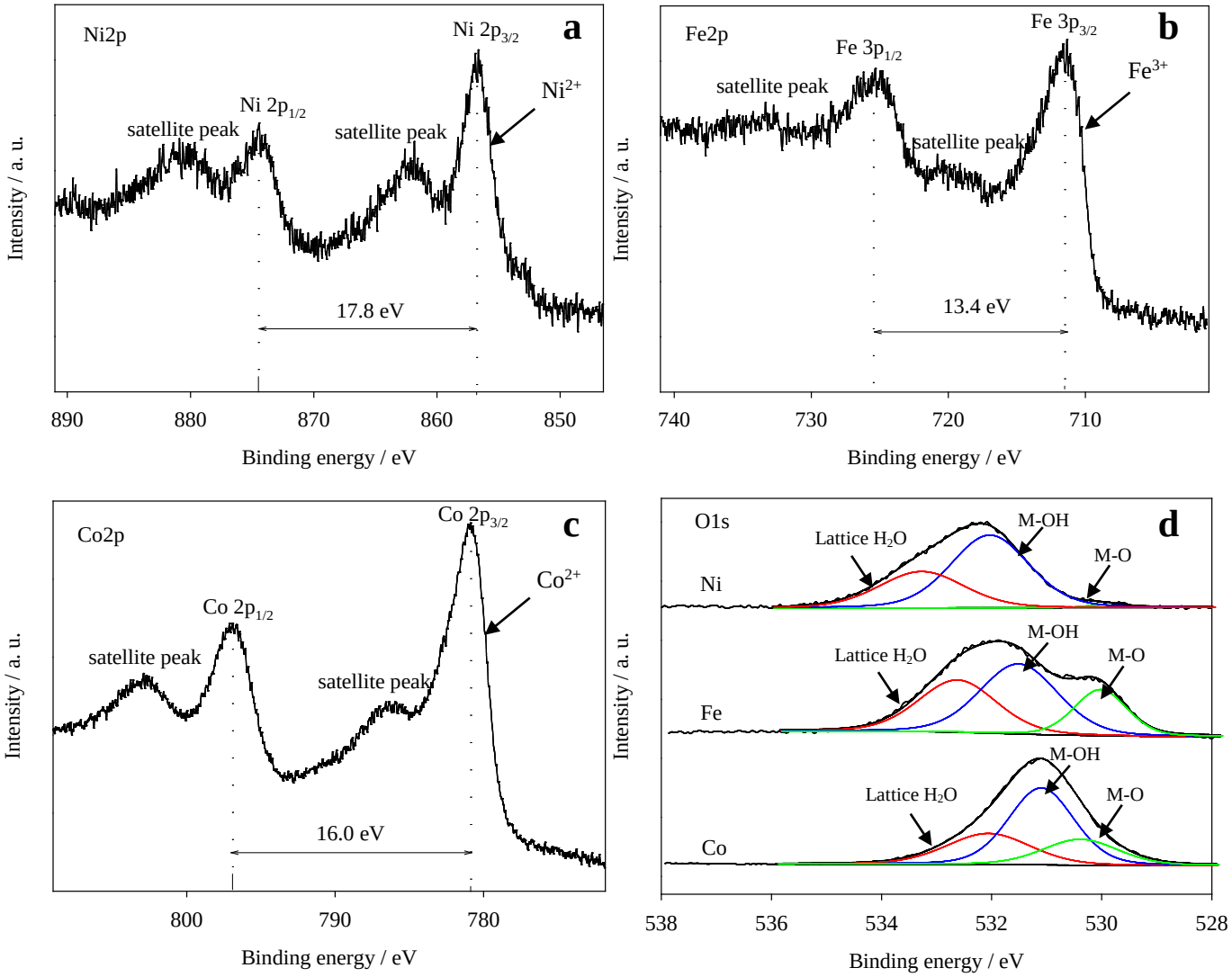
Ni2p
a
Ni 2p3/2
Ni2+
Ni 2p1/2
satellite peak
satellite peak
17.8 eV
Intensity / a. u.
890
880
870
860
850
Binding energy / eV
Fe2p
b
Fe 3p3/2
Fe 3p1/2
Fe3+
satellite peak
satellite peak
13.4 eV
Intensity / a. u.
740
730
720
710
Binding energy / eV
Co2p
c
Co 2p3/2
Co2+
Co 2p1/2
satellite peak
satellite peak
16.0 eV
Intensity / a. u.
800
790
780
Binding energy / eV
O1s
d
Lattice H2O
M-OH
M-O
Ni
Fe
Co
Intensity / a. u.
538
536
534
532
530
528
Binding energy / eV

Fig. 4

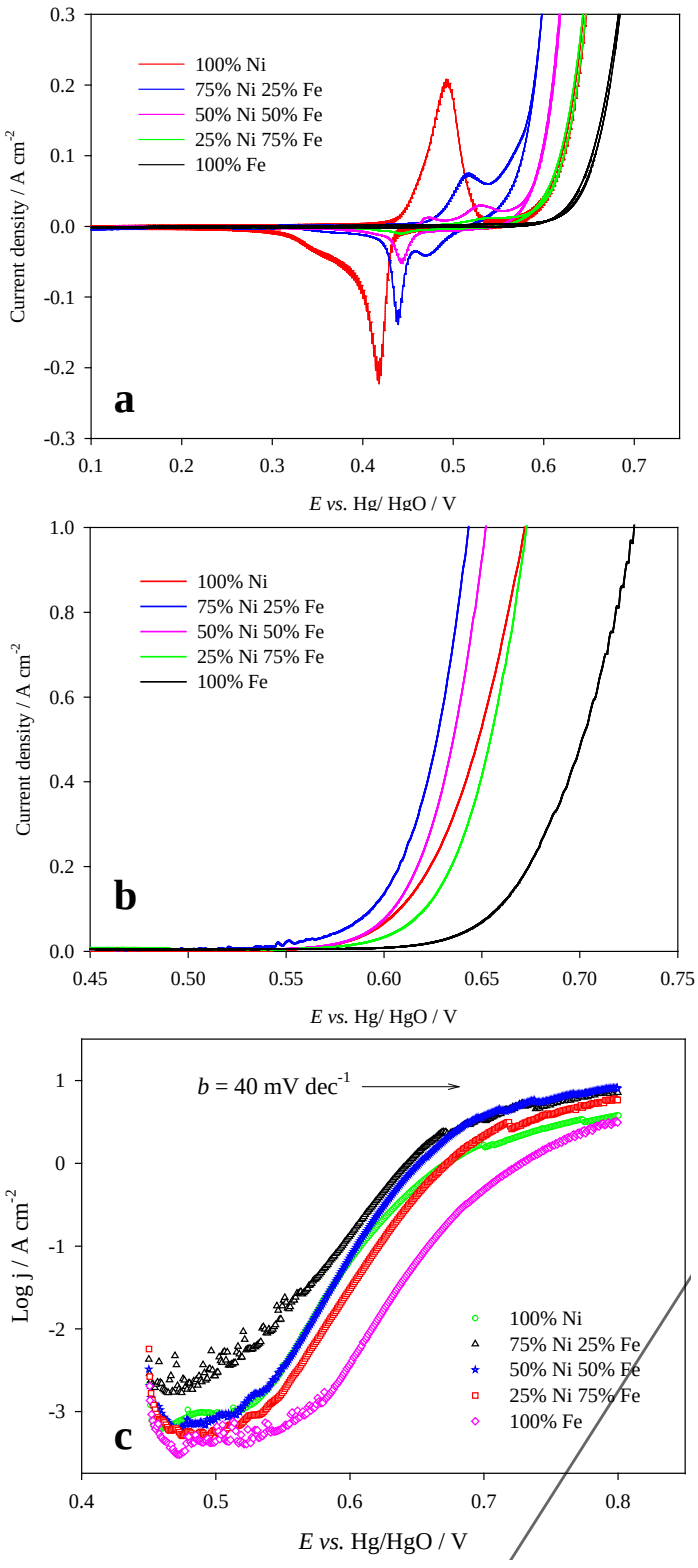
100% Ni
75% Ni 25% Fe
50% Ni 50% Fe
25% Ni 75% Fe
100% Fe
Current density / A cm-2
E vs. Hg/ HgO / V
a
b
b = 40 mV dec-1
Log j / A cm-2
E vs. Hg/HgO / V
c

Fig. 5

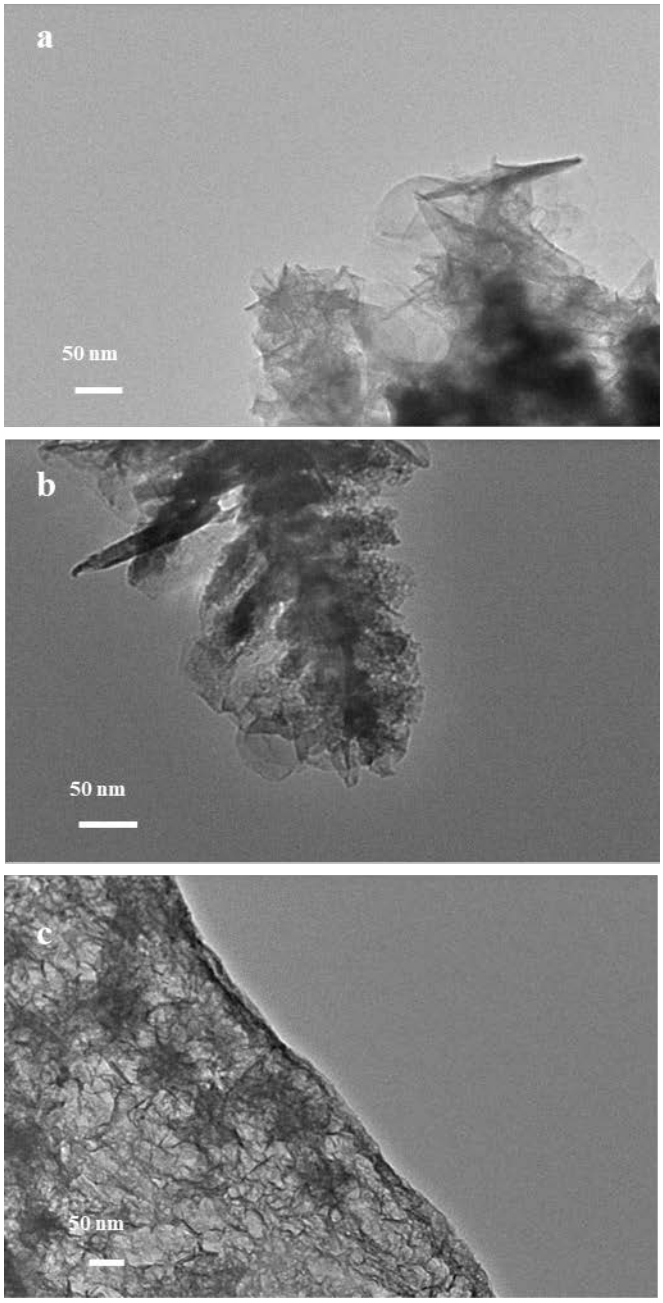

Fig. 6

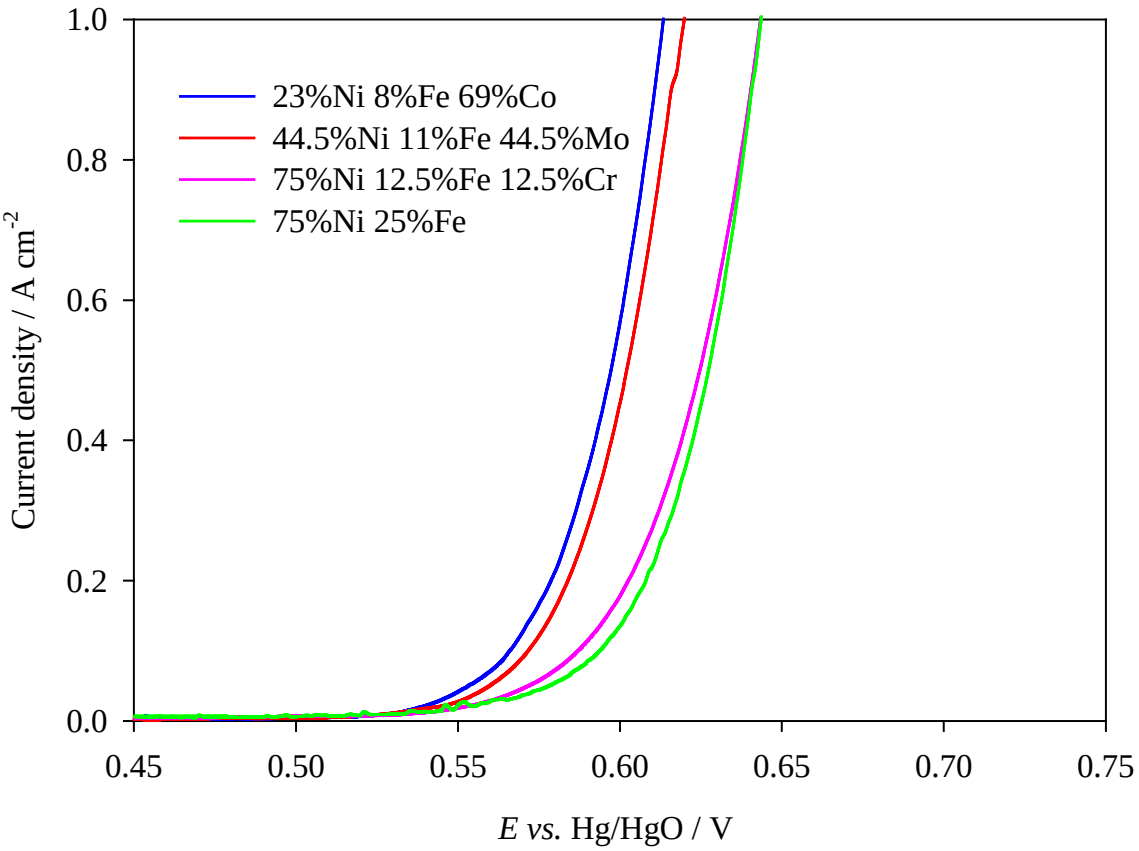
1.0
0.8
0.6
0.4
0.2
0.0
0.45
0.50
0.55
0.60
0.65
0.70
0.75
Current density / A cm-2
E vs. Hg/HgO / V
23%Ni 8%Fe 69%Co
44.5%Ni 11%Fe 44.5%Mo
75%Ni 12.5%Fe 12.5%Cr
75%Ni 25%Fe

Fig. 7

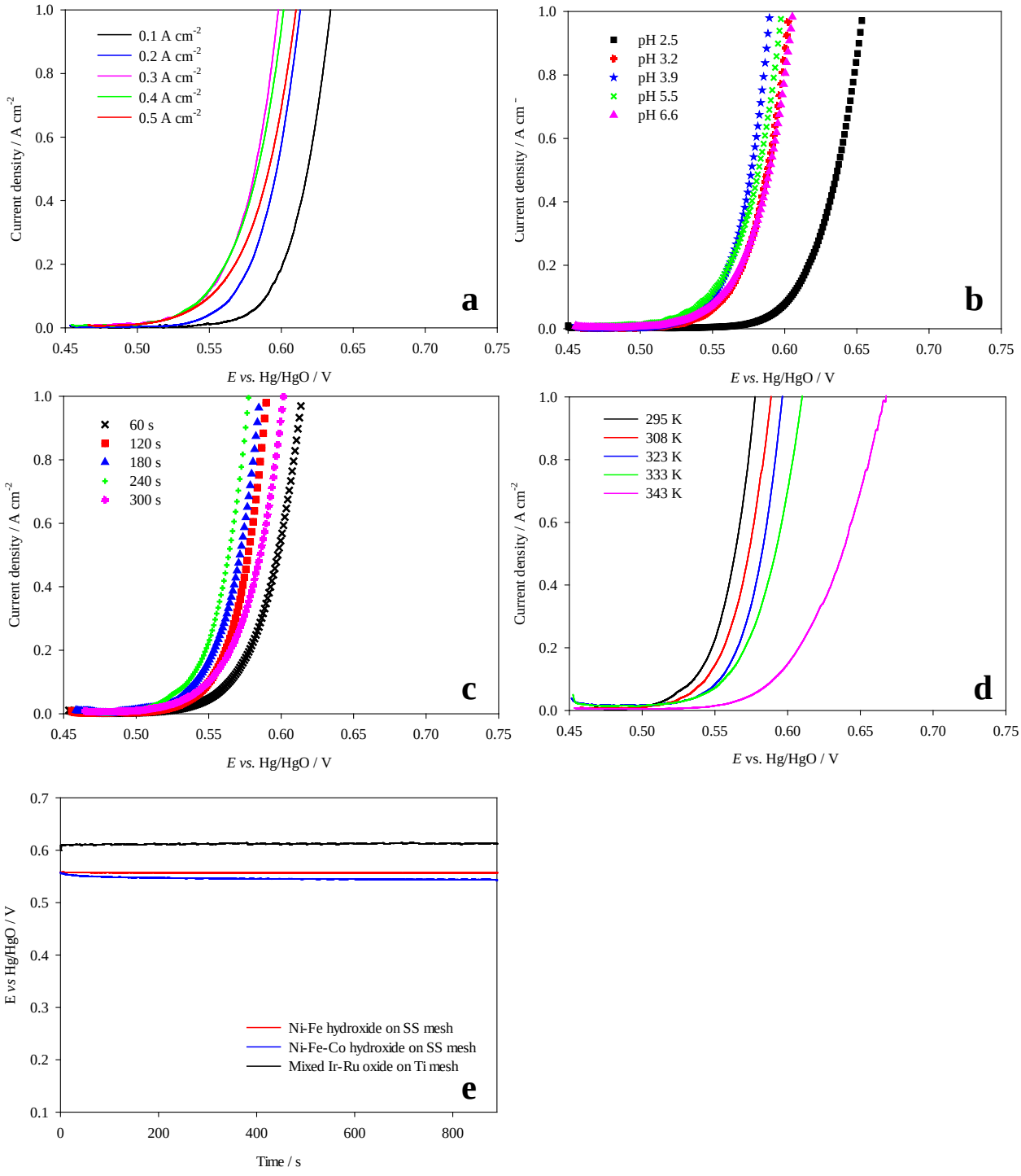
0.1 A cm-2
0.2 A cm-2
0.3 A cm-2
0.4 A cm-2
0.5 A cm-2
Current density / A cm-2
E vs. Hg/HgO / V
a
pH 2.5
pH 3.2
pH 3.9
pH 5.5
pH 6.6
Current density / A cm-2
E vs. Hg/HgO / V
b
60 s
120 s
180 s
240 s
300 s
Current density / A cm-2
E vs. Hg/HgO / V
c
295 K
308 K
323 K
333 K
343 K
Current density / A cm-2
E vs. Hg/HgO / V
d
Ni-Fe hydroxide on SS mesh
Ni-Fe-Co hydroxide on SS mesh
Mixed Ir-Ru oxide on Ti mesh
E vs Hg/HgO / V
Time / s
e

Fig. 8

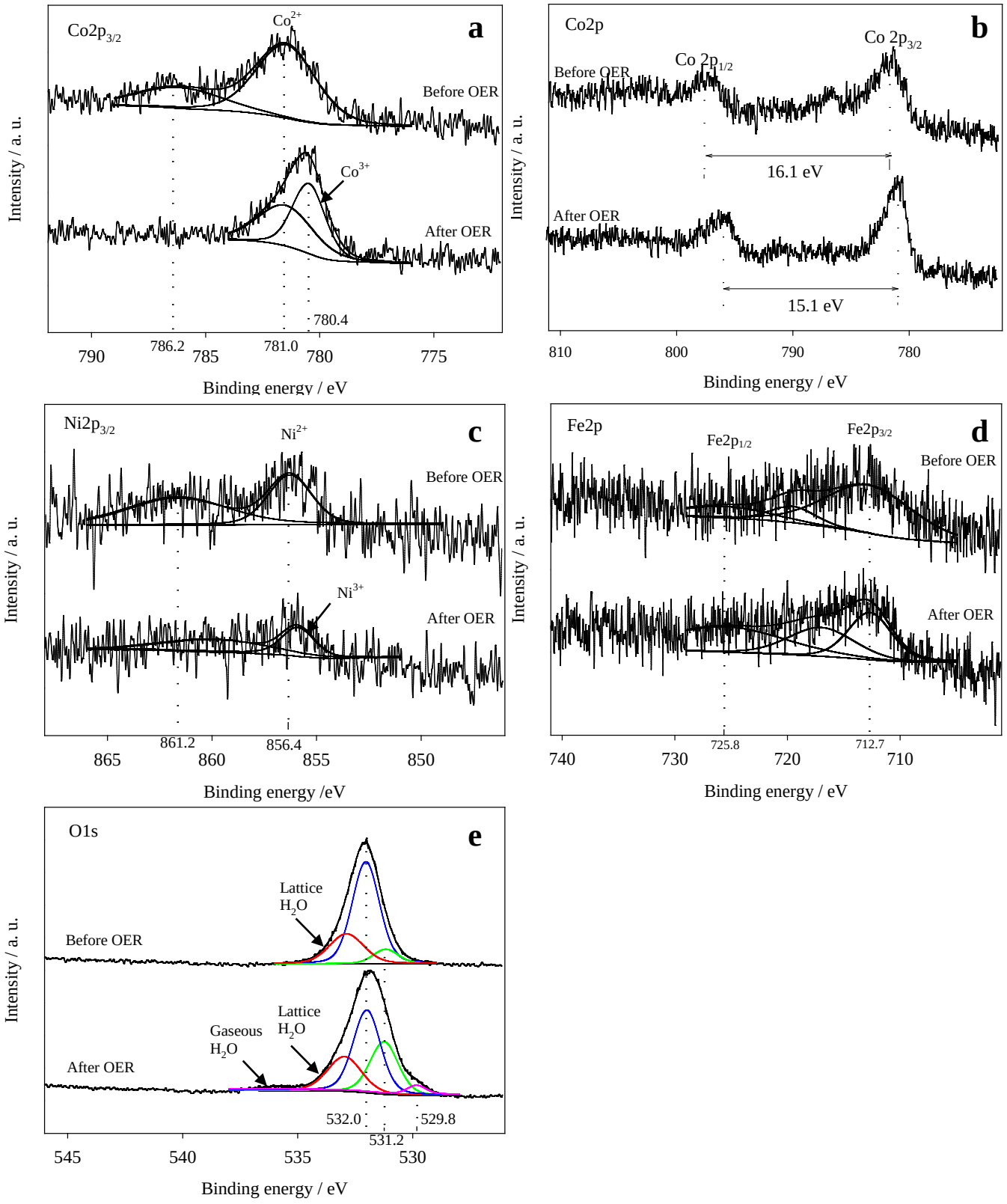
Co2p3/2
Co2+
a
Before OER
Co3+
After OER
780.4
786.2
781.0
790
785
780
775
Intensity / a. u.
Binding energy / eV
Co2p
b
Co 2p1/2
Co 2p3/2
Before OER
16.1 eV
After OER
15.1 eV
810
800
790
780
Intensity / a. u.
Binding energy / eV
Ni2p3/2
Ni2+
c
Before OER
Ni3+
After OER
861.2
856.4
865
860
855
850
Intensity / a. u.
Binding energy /eV
Fe2p
Fe2p1/2
Fe2p3/2
d
Before OER
After OER
725.8
712.7
740
730
720
710
Intensity / a. u.
Binding energy / eV
O1s
e
Lattice H2O
Before OER
Gaseous H2O
Lattice H2O
After OER
532.0
531.2
529.8
545
540
535
530
Intensity / a. u.
Binding energy / eV

Fig. 9

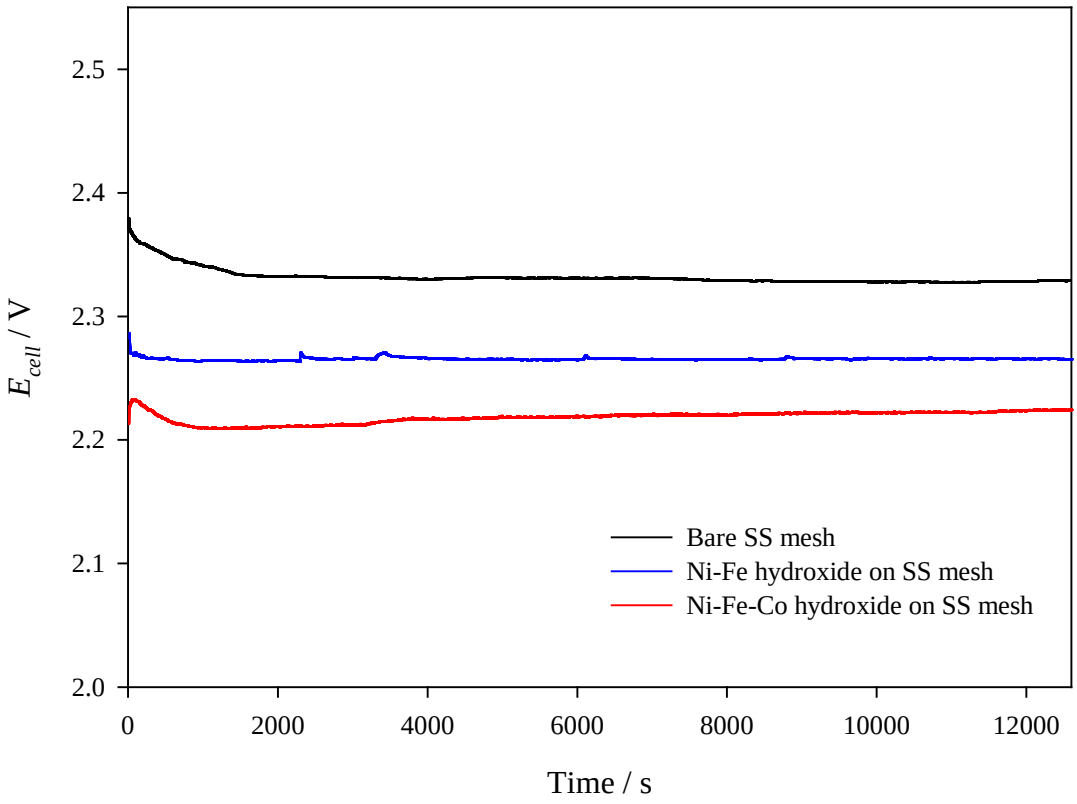
2.5
2.4
2.3
2.2
2.1
2.0
E_{cell} / V
0
2000
4000
6000
8000
10000
12000
Time / s
Bare SS mesh
Ni-Fe hydroxide on SS mesh
Ni-Fe-Co hydroxide on SS mesh

Fig. 10